Coastal Engineering 160 (2020) 103744

Contents lists available at ScienceDirect

Coastal Engineering

journal homepage: http://www.elsevier.com/locate/coastaleng

Wave loads on a land-based dual-chamber Oscillating Water Column wave energy device

Rong-quan Wang [a], De-zhi Ning [a,*], Qing-ping Zou [b]

[a] State Key Laboratory of Coastal and Offshore Engineering, Dalian University of Technology, Dalian, 116024, China
[b] The Lyell Centre for Earth and Marine Science and Technology, Institute for Infrastructure and Environment, Heriot-Watt University, Edinburgh, EH14 4AS, UK

ARTICLE INFO

Keywords:
Dual-chamber OWC
Wave loads
Wave moment
Wave energy
HOBEM

ABSTRACT

Wave energy is one of renewable energy resources with great potential. Due to the mechanical and structural simplicity, Oscillating Water Column (OWC) Wave Energy Converter (WEC) is considered to be one of the most promising marine renewable energy devices. However, OWC remains not commercialized mainly due to its complex hydrodynamic performance and uncertainty in wave loads. In the present study, based on potential flow theory and time-domain higher-order boundary element method (HOBEM), a fully nonlinear numerical model is developed and used to investigate the wave-induced force and bending moment on a land-fixed dual-chamber OWC device. The Bernoulli equation is used to calculate the wave force and bending moment. The equation is modified by accounting for the pneumatic pressure in the air chamber and the viscosity effect and then solved using an acceleration-potential method. The numerical model was compared with the experiment carried out in a wave-current flume at the State Key Laboratory of Coastal and Offshore Engineering, Dalian University of Technology, China, and good agreement between the simulation and experimental results was observed. The horizontal components of wave forces on the two curtain walls of the dual-chamber OWC WEC were found to be much larger than the corresponding vertical components. The seaside curtain wall suffered much larger wave loads in comparison with the inner curtain wall. Therefore, the wave force on the seaside curtain wall is the dominant force. The largest wave-induced bending moment occurs at the joint of device and seabed. The effects of the sub-chamber width ratio and curtain-wall draft on the wave-induced force and bending moment are investigated. The dominant wave force and moment increase with curtain wall draft. And the peak wave loads can be reduced by moving the internal curtain wall close to the seaside curtain wall.

1. Introduction

As one of renewable energy sources, wave energy is of great potential and stands out by its high energy density, well-predictability (Arena et al., 2015) and low environmental impact (Iglesias and Carballo, 2014). Numerous types of wave energy converters (WECs) have been proposed and developed in the past decades to harness wave power. However, compared with other renewable clean energy technologies, such as solar, wind and tidal energy, the technology of utilization wave energy is still immature (Sheng, 2019; Zheng et al., 2019), and few WECs have achieved a commercial stage (López et al., 2020). Among different types of WECs, Oscillating Water Column (OWC) devices hold a prominent position for its mechanical and structural simplicity (Falcão and Henriques, 2016). Generally, an OWC device consists of a partially immersed chamber with an air pocket trapped over a water column. The wave-induced up and down motion of the water column forces the air inside the chamber to be compressed and expanded. Then, such a reciprocating air flow is produced through an orifice/vent connected to an air turbine. Finally, the electricity is produced by a generator driven by the turbine. Several full-scale prototype OWC devices have been built and tested, including OSPREY plant (1 MW, 1995) in UK, Pico plant (400 kW, 1999) in Portugal, Shawnee OWC plant (100 kW, 2001) in China, Mutriku OWC breakwater in Spain (300 kW, about 2008), greenWAVE (1 MW, 2014) in Australia and Yonsei OWC plant (500 kW, 2015) in South Korea.

The OWC devices have been widely investigated in the past few decades (Wang et al., 2018; Xu and Huang, 2019) with majority attentions to optimize the device geometrical parameters to improve its hydrodynamic performance (Deng et al., 2019a, 2020; Kamath et al., 2015; Vyzikas et al., 2017a, 2017b; Zhou et al., 2018). The concept of

* Corresponding author.
E-mail address: dzning@dlut.edu.cn (D.-z. Ning).

https://doi.org/10.1016/j.coastaleng.2020.103744
Received 10 December 2019; Received in revised form 29 May 2020; Accepted 7 June 2020
Available online 23 June 2020
0378-3839/© 2020 The Authors. Published by Elsevier B.V. This is an open access article under the CC BY-NC-ND license (http://creativecommons.org/licenses/by-nc-nd/4.0/).

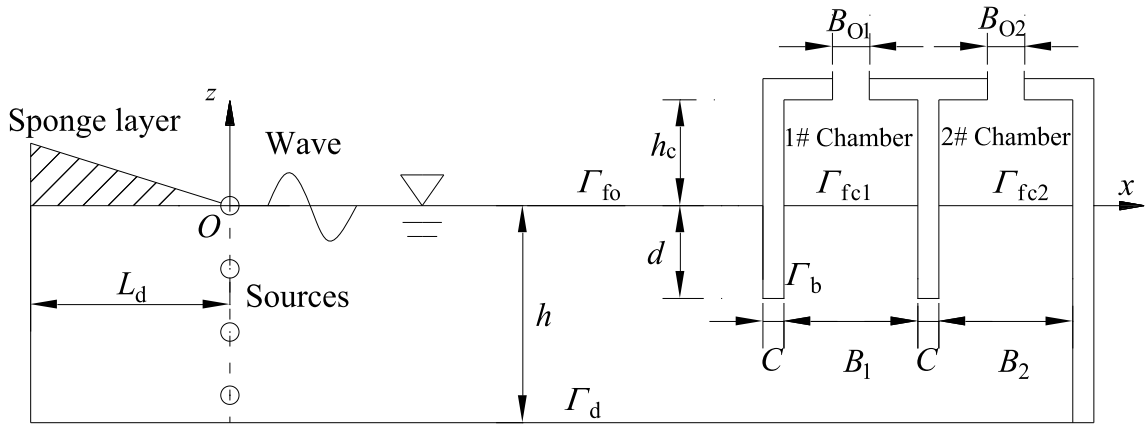

Fig. 1. Sketch of the numerical model set-up.

dual-chamber OWC device was proposed and developed recently (Elhanafi et al., 2018; Ning et al., 2018; Wang et al., 2017). It was found that capture width ratio and effective frequency bandwidth of the OWC device can be improved by introducing a dual-chamber structure (Ning et al., 2019; Rezanejad et al., 2015). High energy conversion efficiency and reliability of WEC devices are the two most important considerations when a WEC device is designed and constructed. Hydrodynamic loads have a remarkable effect on the subsurface structure of marine renewable energy converters (Liu et al., 2018) and determine the device safety. However, the study of hydrodynamic force and moment on OWC devices is still lack. This may be due to the fact that most of the OWC devices were land-based and the reliability was taken for granted. Relatively little attentions have been paid to floating OWC devices with a mooring system which experienced a more complex hydrodynamic environment (Elhanafi, 2016; He et al., 2019; Hong et al., 2004a, 2004b; Iturrioz et al., 2014; Konispoliatis and Mavrakos, 2016; Koo, 2009), not to mention the bottom-mounted type OWC device. However, several prototype OWC devices have been damaged by storms. The bottom-fixed nearshore plants OSPREY and greenWAVE were destroyed during disastrous deployment operations in 1995 and 2014, respectively (Falcão and Henriques, 2016). The concrete submerged structure of the Pico plant was significantly damaged by waves (Monk, 2015) and the structure foundation of the plant eventually collapsed due to a strong storm in 2018 (Falcão et al., 2018). The Mutriku plant suffered severe damages from storms during its construction (Medina-Lopez et al., 2015).

Not until recent years did investigations of hydrodynamic forces on bottom-mounted OWC devices start. The wave forces on the caisson breakwaters embodying a U-OWC was numerically investigated by Boccotti (2012). Based on smoothed particle hydrodynamics (SPH) method, Didier et al. (2016) calculated the wave forces on the OWC front wall and investigated the influence of the wave height on the forces. Viviano et al. (2016) experimentally investigated the wave forces acting on the OWC device under random waves. They computed the forces on the front wall by integrating the measured pressure on the surfaces of the wall and found that the force formula for vertical walls are not valid for OWC devices. Later, Viviano et al. (2018) further investigated the scaling effect on the wave force, and Viviano et al. (2019) investigated the wave pressure on front wall of a OWC device under the regular waves. Ashlin et al. (2015) conducted experimental studies of dynamic pressure and total wave force on the OWC device and found that the total horizontal wave force was 2.5–3 times larger than the total vertical force. Ning et al. (2016a) experimentally and numerically analyzed the effects of chamber parameters and wave conditions on wave force exerted on the OWC device and reported that the horizontal wave force increases with wave height and decreases with wavelength. Then, the viscosity effects on the wave force were systemically analyzed by Wang and Ning (2020). Huang et al. (2019) performed a three-dimensional (3-D) numerical simulation of the wave load on an OWC-pile device. They reported that the horizontal and vertical wave forces and the moment are insensitive to wave period, but increase with wave height. Recently, a numerical model was constructed by Pawitan et al. (2019) to estimate the wave forces on a caisson OWC-breakwater based on large scale observations. The vertical force on the chamber ceiling was found to have a significant influence on overturning and sliding of the breakwater. These investigations are mainly focused on total wave force on a single-chamber OWC device. Due to the special structure of the OWC device, the curtain walls of the chamber suffered not only the force from the waves, but also the pressure from the inner chamber. In addition, the free surface motion inside OWC chamber may become a sloshing mode during certain wave conditions, leading to a larger wave force on the inside surface of the chamber wall (Ning et al., 2016b; Xue et al., 2017, 2019). Thus, characteristics of individual wave force components worth comprehensive studying besides total wave force. As reported by Ning et al. (2016a), seaward wave force components may cause damage from the inner side of the device and wave moment could induce an overturning of the device just as what happened to the Pico plant.

Ning et al. (2019) experimentally investigated the hydrodynamic performance of a dual-chamber OWC device. As a follow-up study, the present research numerically investigates the wave loads on the dual-chamber device with a special attention to the wave force and bending moment exerted on the device. The characteristics of the wave loads under the influences of sub-chamber width and curtain wall draft are thoroughly examined to optimize the dual-chamber OWC device design and its survivability. The remainder of the present paper is organized as follows. The numerical model is presented in section 2. The experimental set-up to validate the present numerical model is described in Section 3. Validations of the numerical model are described in Section 4. Section 5 is dedicated to the characteristics of wave-induced force and bending moment and the effects of sub-chamber width ratio and curtain wall draft on wave loads. Final conclusions are summarized in Section 6.

2. Numerical modeling

The numerical model, which based on potential flow theory and the time-domain higher-order boundary element method (HOBEM), developed by Ning et al. (2016a) to describe the wave dynamics on a single-chamber OWC is extended here to examine the wave loads on a dual-chamber OWC device. The sketch of the numerical model is depicted in Fig. 1. A 2-D Cartesian coordinate system (O-xz) is chosen with its origin (0, 0) on the static water surface. As shown in Fig. 1, B_1 and B_2 are the widths of the 1# and 2# chamber, respectively; B_{O1} and B_{O2} are the widths of the 1# and 2# orifice, respectively; C and d are the thickness and draft of the two curtain walls, i.e., 1# seaside curtain wall and 2# inner curtain wall, respectively (note that both the thickness and

draft of the two curtain walls are assumed to be equal to each other in this study); h denotes the water depth and h_c the air chamber height; L_d denotes the sponge layer length.

It is assumed that the fluid is inviscid, incompressible, and the fluid flow is irrotational. Thus, the fluid motion can be described by the velocity potential φ and the governing Laplace equation is satisfied. To avoid wave re-reflection, the inner sources technique is adopted here to generate incident wave and a sponge layer with a damping coefficient $\nu(x)$ is added at the left end of the wave flume to absorb the reflected waves. Then, the governing equation is changed to the Poisson equation. To model the energy loss due to vortex shedding and flow separation near the dual-chamber OWC device, artificial viscous terms with damping coefficients μ_1 and μ_2 are added to the dynamic free-surface boundary conditions in 1# and 2# chamber, respectively (Ning et al., 2015, 2016a). The MEL (mixed Eulerian–Lagrangian) approach and the RK4 (4th-order Runge–Kutta) integration scheme are used to update the fully nonlinear dynamic and kinematic free-surface conditions at each time step. Thus, the free-surface boundary conditions are then written as:

$$\begin{cases} \dfrac{dX(x,z)}{dt} = \nabla\varphi - \upsilon(x)(X - X_0) \\ \dfrac{d\varphi}{dt} = -g\eta + \dfrac{1}{2}(\nabla\varphi\cdot\nabla\varphi) - \upsilon(x)\varphi, \quad outside \;\; the \;\; chambers \\ \dfrac{d\varphi}{dt} = -g\eta + \dfrac{1}{2}(\nabla\varphi\cdot\nabla\varphi) - \dfrac{p_{a1}}{\rho} - \mu_1\dfrac{\partial\varphi}{\partial n} \;\; , \;\; in \;\; 1\# \;\; chamber \\ \dfrac{d\varphi}{dt} = -g\eta + \dfrac{1}{2}(\nabla\varphi\cdot\nabla\varphi) - \dfrac{p_{a2}}{\rho} - \mu_2\dfrac{\partial\varphi}{\partial n} \;\; , \;\; in \;\; 2\# \;\; chamber \end{cases}, \tag{1}$$

in which $d/dt = \partial/\partial t + \nabla\varphi\cdot\nabla$ is the material derivative; $\boldsymbol{X}(x, z)$ denotes position vector of a fluid particle on the free surface, and $\boldsymbol{X_0}(x_0, 0)$ the initial static position of a fluid particle; η denotes the free surface elevation, n the normal vector with its positive direction outward from the fluid domain, t the time, g the gravitational acceleration and ρ the water density; μ_1 and μ_2 are the artificial viscous damping coefficients in 1# and 2# chamber, respectively. The damping coefficient of the sponge layer $\nu(x)$ is given by

$$\upsilon(x) = \begin{cases} \omega(x - x_1)^2 L_d^{-2}, & x_1 - L_d < x < x_1 \\ 0, & x \geq x_1 \end{cases}, \tag{2}$$

where ω is the angular frequency, L_d is the length of the sponge layer with its length of 1.5λ (where λ is the wavelength), and x_1 is the starting position of sponge layer.

p_{a1} and p_{a2} are the air pressures due to water motion in 1# and 2# chamber, respectively. Assuming a quadric relationship between air pressure and airflow velocity, the air pressures are given by:

$$\begin{cases} p_{a1}(t) = D_{dm1}|U_{d1}(t)|U_{d1}(t), \;\; in \;\; 1\# \;\; chamber \\ p_{a2}(t) = D_{dm2}|U_{d2}(t)|U_{d2}(t), \;\; in \;\; 2\# \;\; chamber \end{cases}, \tag{3}$$

in which D_{dm1} and D_{dm2} denote the quadric pneumatic damping coefficients of 1# and 2# orifice, respectively; U_{d1} and U_{d2} denote the airflow velocities through 1# and 2# orifice, respectively. It was reported that the air compressibility effects may lead to errors when the small-scale results were extrapolated to full-scale (Falcão and Henriques, 2014). And the air compressibility effects are found to be highly influenced by the wave period (López et al., 2020). Simonetti et al. (2018) found that there is about a 15% overestimation of the air pressure due to the neglecting air compressibility in a 1: 50 model scale when compared to the full-scale model. However, the present study aims to reproduce the small-scale experiments as the air compressibility plays negligible roles in the small scaled model testing as presented in (Elhanafi et al., 2017). It follows that the airflow velocities U_{d1} and U_{d2} can be calculated as follows:

$$\begin{cases} U_{d1}(t) = \dfrac{\Delta V_1}{S_{O1}\Delta t}, \;\; in \;\; orifice \;\; 1 \\ U_{d2}(t) = \dfrac{\Delta V_2}{S_{O2}\Delta t}, \;\; in \;\; orifice \;\; 2 \end{cases}, \tag{4}$$

in which $\Delta V_1 = V_{1(t+\Delta t)}$-$V_{1t}$ and $\Delta V_2 = V_{2(t+\Delta t)}$-$V_{2t}$ denote the change of volume of water columns in 1# and 2# chamber within each time step Δt, respectively. S_{O1} and S_{O2} are the cross-section areas of 1# and 2# orifice, respectively, as illustrated in Fig. 1.

To solve the above problem in the time domain, the impermeable condition on solid boundary and initial clam water surface conditions need to be satisfied:

$$\begin{cases} \dfrac{\partial\varphi}{\partial n} = 0, \;\; on \;\; \Gamma_b \;\; and \;\; \Gamma_d \\ \varphi|_{t=0} = \eta|_{t=0} = 0 \end{cases}. \tag{5}$$

By applying the second Green's theorem to the computation domain Ω, the following boundary integral equation can be obtained:

$$\alpha(p_s)\varphi(p_s) = \int_\Gamma \left[\varphi(p_f)\frac{\partial G(p_s,p_f)}{\partial n} - G(p_s,p_f)\frac{\partial\varphi(p_f)}{\partial n}\right]d\Gamma + \int_\Omega q^* G(p_s,p_f)d\Omega, \tag{6}$$

in which Γ denotes the computational boundary, including Γ_{fO}, Γ_{fc1}, Γ_{fc2} and Γ_b; G denotes the simple Green function; α is the solid angle

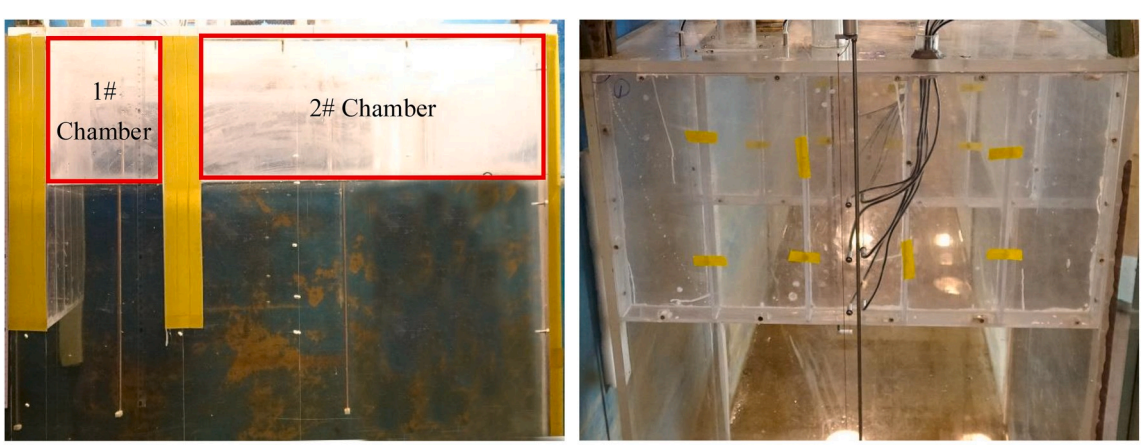

(a) Dual-chamber OWC model (b) Pressure gauge distribution

Fig. 2. A view of the (a) dual-chamber OWC model installed in the wave-current flume and (b) the pressure gauge distributed on the curtain walls.

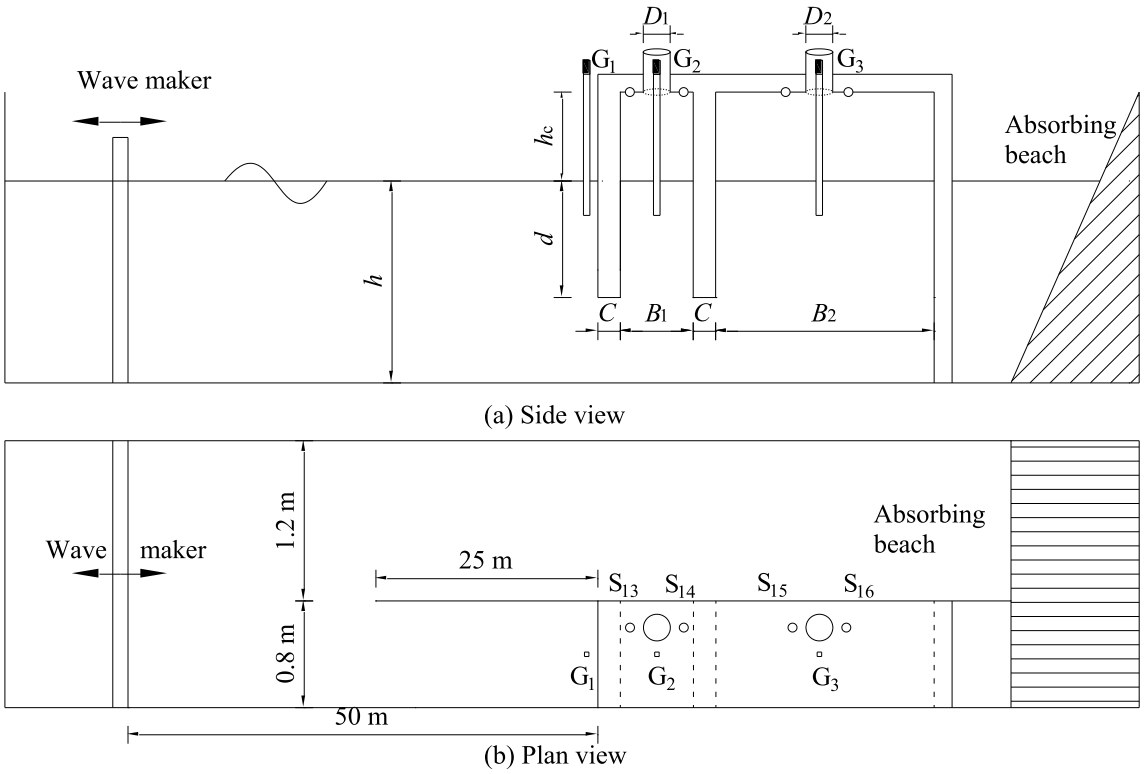

Fig. 3. Sketch of the experimental setup in the wave flume. G_1 to G_3: wave gauges; S_{13} to S_{16}: pressure sensors.

coefficient; p_s (x_0, z_0) and p_f (x, z) represent the source and field point, respectively.

The velocity potential on the OWC structure surface is obtained once Eq. (6) is solved. Then, based on Bernoulli equation, the wave-induced pressure on the OWC device can be obtained. Finally, the wave-induced force $\boldsymbol{F}$ and bending moment $\boldsymbol{M}$ can be calculated by integrating the wave pressure over the instantaneous wetted OWC device surface (Γ_b) as

$$\boldsymbol{F} = \int_{\Gamma_b} p_w \boldsymbol{n} \mathrm{d}\Gamma = -\rho \int_{\Gamma_b} \left[\frac{\partial \varphi}{\partial t} + g\eta + \frac{1}{2}(\nabla\varphi \cdot \nabla\varphi) + \frac{p_a}{\rho} - \mu \frac{\partial \varphi}{\partial t} \right] \boldsymbol{n} \mathrm{d}\Gamma, \tag{7}$$

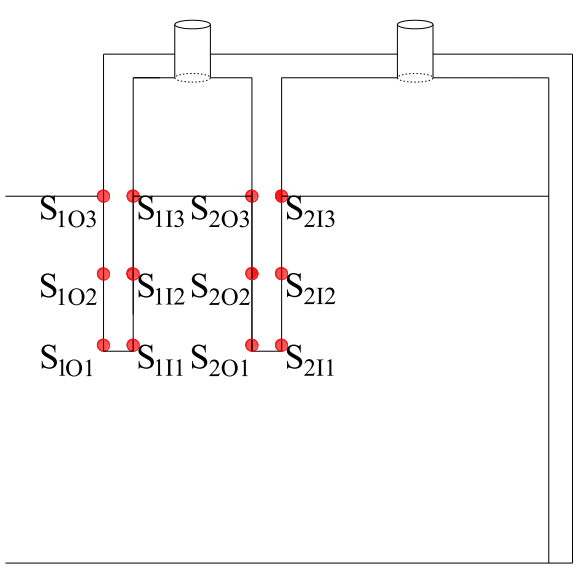

Fig. 4. Distribution of the pressure sensors on the two curtain walls of the dual-chamber OWC model.

$$\begin{aligned} \boldsymbol{M} &= \int_{\Gamma_b} p_w (\boldsymbol{r} \times \boldsymbol{n}) \mathrm{d}\Gamma \\ &= -\rho \int_{\Gamma_b} \left[\frac{\partial \varphi}{\partial t} + g\eta + \frac{1}{2}(\nabla\varphi \cdot \nabla\varphi) + \frac{p_a}{\rho} - \mu \frac{\partial \varphi}{\partial t} \right] (\boldsymbol{r} \times \boldsymbol{n}) \mathrm{d}\Gamma, \end{aligned} \tag{8}$$

in which p_w denotes the wave induced pressure on the OWC surface, $\boldsymbol{r}$ denotes the distance vector and $\boldsymbol{r} \times \boldsymbol{n}$ is the length of the moment arm, the pressure term p_a/ρ represents the pneumatic pressure in the chamber. Head loss/pressure drop H_L occurs when wave interactions with the OWC device due to turbulence phenomena such as vortex shedding and flow separations. And the linearized Bernoulli equation $p = \partial\varphi/\partial t$ is used here to consider this influence. Therefore, the last term $\mu\partial\varphi/\partial t$ in Eqs. (7) and (8) is introduced to account for these turbulence effects on the wave force. The time derivative of velocity potential $\partial\varphi/\partial t$ is calculated by using the acceleration-potential method. More details for solving Eqs. (7) and (8) can refer to (Koo and Kim, 2007; Ning et al., 2016a).

3. Experimental setup

The experimental tests were carried out in the wave-current flume at the State Key Laboratory of Coastal and Offshore Engineering, Dalian University of Technology, China with a constant water depth h of 1.0 m. A piston-type unidirectional wave-maker and a wave-absorbing beach are located at the two ends of the flume to generate the desired incident waves and absorb the incoming waves, respectively. The glass-walled wave-current flume is 69 m in length, 2.0 m in width and 1.8 m in depth. The flume was divided into two parallel sections with a width of 1.2 m and 0.8 m, respectively, by a thin vertical wall along the longitudinal direction. The dual-chamber OWC model was placed in the 0.8 m wide section of the flume. To avoid the wave energy transfer through the gap between the device and the flume walls, the spanwise width of the model was chosen to be equal to the width of the flume section, i.e., 0.8 m. Fig. 2 illustrates the photos of the dual-chamber OWC device installed in the wave-current flume.

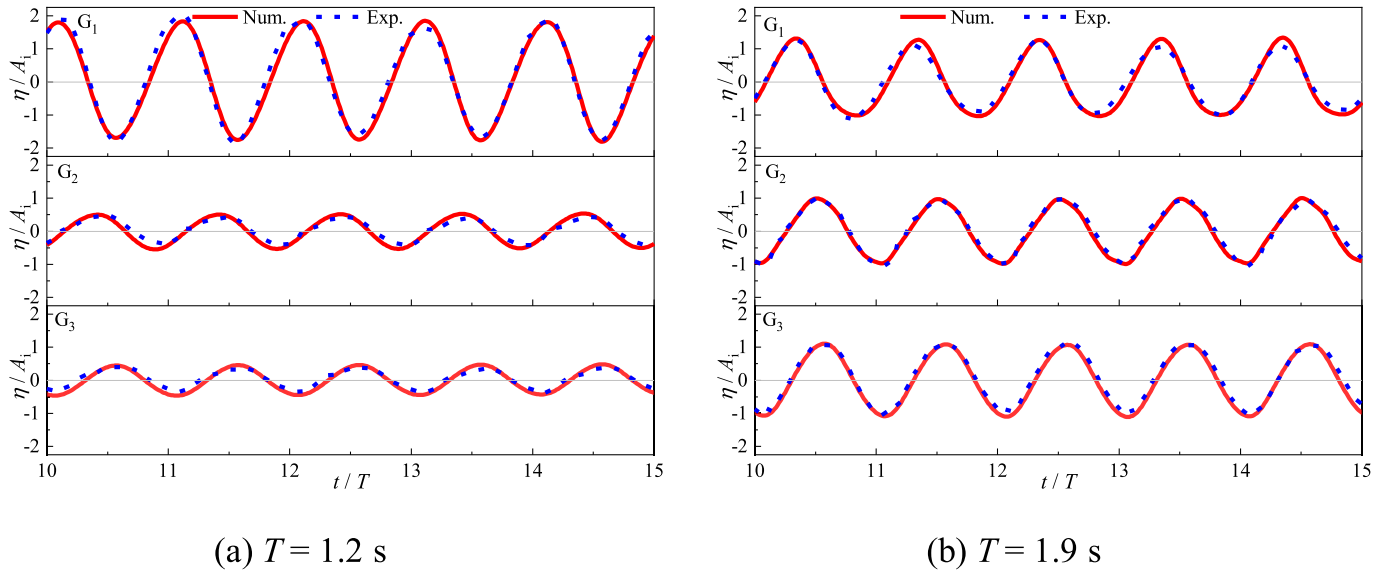

Fig. 5. Time histories of the free surfaces outside (Top) and inside (Middle and Bottom) the chambers for (a) $T = 1.2$ s ($kh = 2.81$) and (b) $T = 1.9$ s ($kh = 1.29$).

According to geometrical similarity, Froude's law of similarity and feasible wave conditions that can be generated in the flume, the model scale was set to 1: 20. Due to proper mechanical strength and transparency of plexiglass, the 18-mm thick perspex sheet was used to make the dual-chamber OWC device model so that the motion of inside free surface can be clearly observed. The sketch of the wave-current flume and the location of dual-chamber OWC model are illustrated in Fig. 3.

Three wave gauges $G_1 \sim G_3$ were used to measure the surface elevations at different locations as shown in Fig. 3. The first gauge G_1 was placed just in front of the device to measure wave runup. The second and third gauges G_2 and G_3 were placed at the centers of 1# and 2# chamber, respectively. In each sub-chamber, there are two pressure sensors mounted near the orifice to measure the pneumatic pressure in the air chamber, i.e., S_{13} and S_{14} in 1# chamber and S_{15} and S_{16} in 2# chamber, as illustrated in Fig. 4. The air pressure together with the surface elevation inside the chamber are used to evaluate the energy extracted from the incident waves. Details of the wave energy absorption characteristics of the dual-chamber OWC can be found in Ning et al. (2019). Twelve pressure sensors were used to measure the wave pressures on 1# and 2# curtain wall with six pressure sensors on each curtain wall. The sensors were evenly and symmetrically distrusted on the seaward and shoreward surfaces of the curtain wall from its bottom edge to the still water surface, i.e., $S_{1O1} \sim S_{1O3}$ and $S_{1I1} \sim S_{1I3}$ on the two surfaces of the 1# curtain wall, respectively; and $S_{2O1} \sim S_{2O3}$ and $S_{2I1} \sim S_{2I3}$ on the two surfaces of the 2# curtain wall, respectively. In order not to distort the flow field around the OWC device, the two curtain walls were made into rectangular boxes to house the pressure sensors to ensure that the outside surface of the curtain walls is smooth as illustrated in Fig. 2(b). All pressure sensors and wave gauges were calibrated immediately before each run to avoid zero drift. Both the pressure (including the air pressure and hydrodynamic pressure) and free surface signals were recorded at a sampling frequency of 50 Hz. Each test case was performed at least two times to reduce the error in measurements, and the averaged value was used in the analysis.

It is well known that power take-off (PTO) plays an important role in power absorption (He and Huang, 2014; He et al., 2017; Ning et al., 2016b). However, it is not practical to simulate PTO system in the present scaled model tests (Rezanejad et al., 2019). Instead, the PTO is

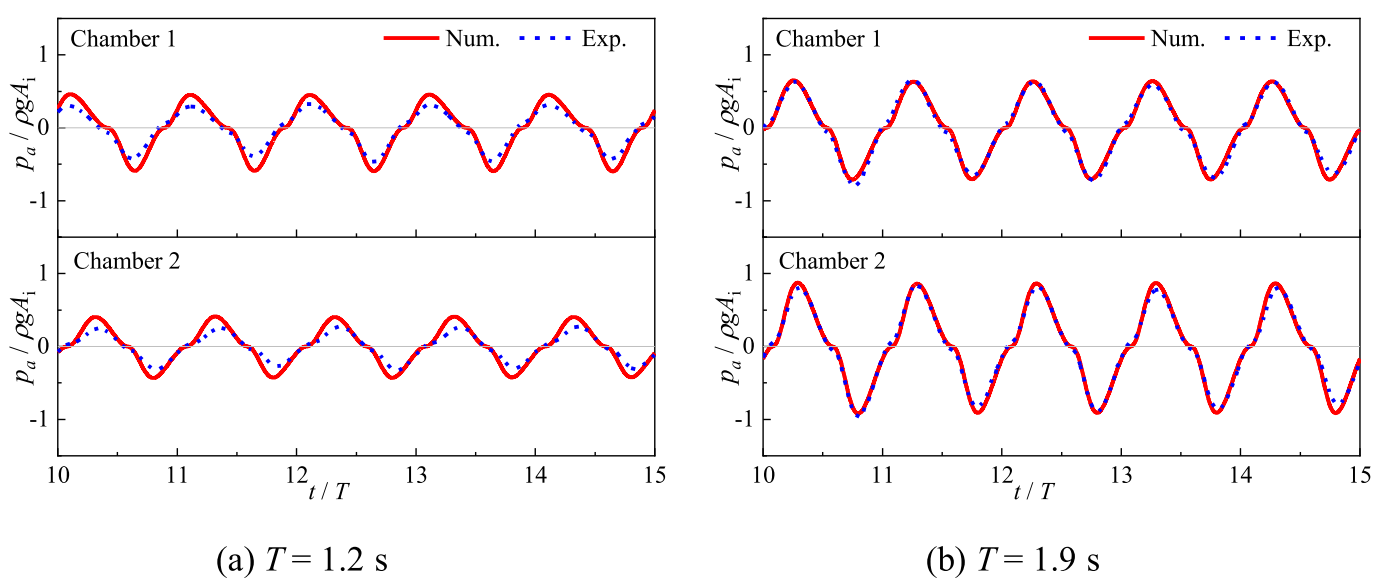

Fig. 6. Time histories of air pressure inside the two sub-chambers for (a) $T = 1.2$ s ($kh = 2.81$) and (b) $T = 1.9$ s ($kh = 1.29$).

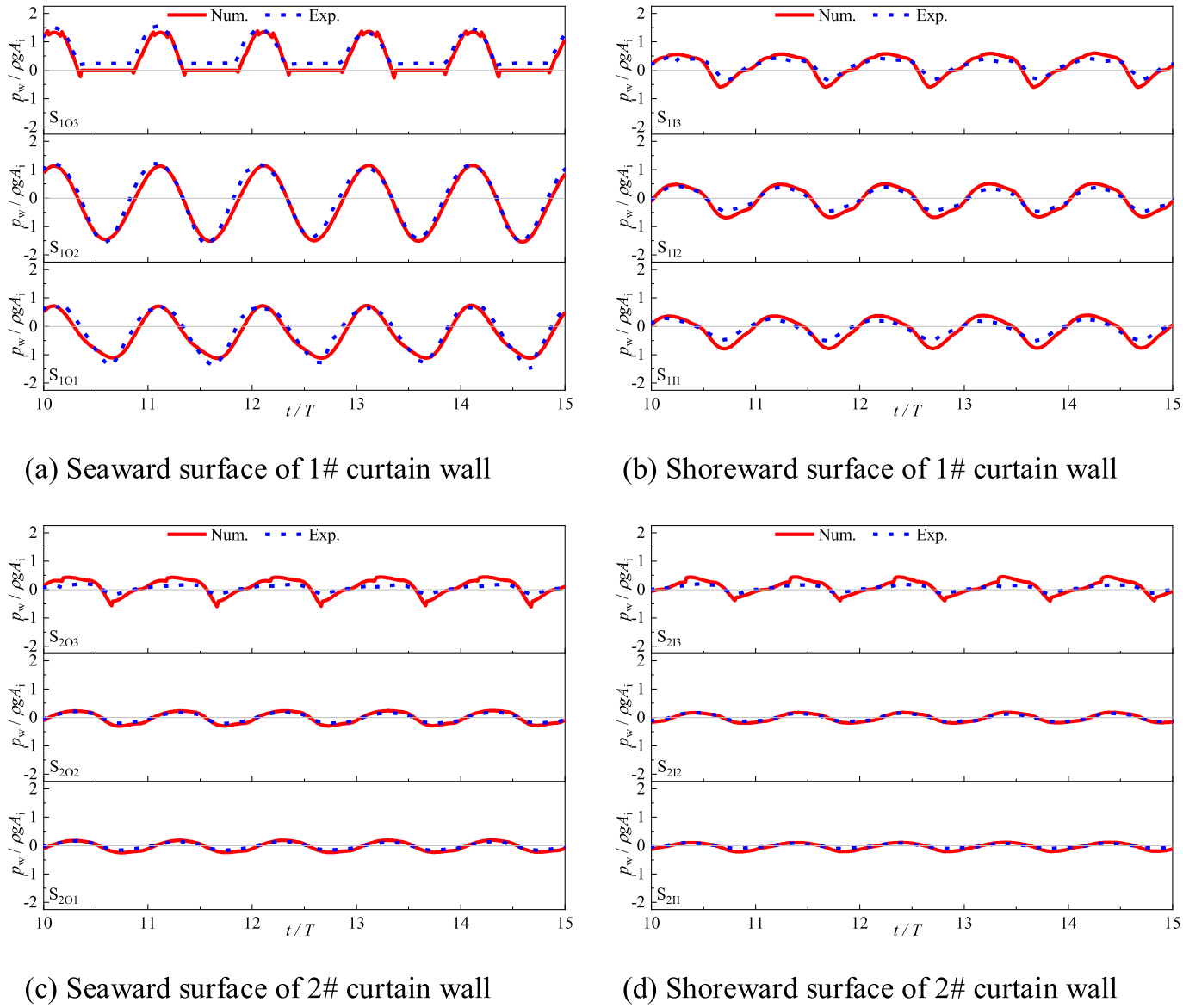

(a) Seaward surface of 1# curtain wall

(b) Shoreward surface of 1# curtain wall

(c) Seaward surface of 2# curtain wall

(d) Shoreward surface of 2# curtain wall

Fig. 7. Time histories of hydrodynamic pressure on the (a) & (c) seaward and (b) & (d) shoreward surfaces of 1# (Upper) and 2# (Lower) curtain walls for $T = 1.2$ s ($kh = 2.81$).

usually mimicked by an orifice located on the air chamber. In the present study, one circular orifice located on each sub-chamber's roof is used as shown in Fig. 3. The optimal opening ratio α ($\alpha = S/S_0$, where S_0 and S are the cross-sectional areas of the still water free surface inside the chamber and the orifice) for a rectangular chamber was found to be in the range of 0.6% ~ 0.7%, 0.66%, and 0.65% respectively by John Ashlin et al. (2016), Ning et al. (2016b) and Deng et al. (2019b). To optimize the performance of the dual-chamber OWC device, a constant optimized opening ratio of $\alpha = 0.66\%$ was adopted for both orifices of the sub-chambers in the present study. The thicknesses of the curtain walls C were set to 0.05 m to house the pressure sensors properly and the chamber height $h_c = 0.2$ m was kept constant. By keeping the total chamber width $B_1 + B_2 + C = 0.7$ m and the curtain wall draft $d = 0.2$ m constants, three sets of sub-chamber width ratios (i.e., B_1: B_2 = 3: 1, 1: 1 and 1: 3) were considered to evaluate the corresponding effect on the hydrodynamic pressure on curtain walls. To ensure the device operation at optimal conditions, the diameters of two circular orifices (i.e., D_1 and D_2) were adjusted with the corresponding chamber width to maintain the optimal opening ratio $\alpha = 0.66\%$. Then, three different curtain wall drafts $d = 0.125$, 0.20 and 0.25 m were tested for a fixed sub-chamber width ratio B_1: B_2 = 1: 1. The wave amplitude in the tests was set to $A_{in} = 0.03$ m and the wave period T ranged from 1.0 s to 2.3 s, with the scale factor of 1: 20. These correspond to the wave conditions: wave height of 1.2 m and wave period of (4.47 ~ 10.28) s in full-scale, hence, align with real sea states in China East seas where the significant wave height ranges from 1 m to 2 m and wave period from 4 s to 6 s (Liang et al., 2014).

4. Physical tests and numerical model validations

Physical tests were performed to (1) validate the dual-chamber OWC numerical model based on fully nonlinear potential flow theory, and (2) test the modified Bernoulli equation for estimating the wave force and bending moment on the dual-chamber OWC device. The validations were carried out for the free-surface elevation outside and inside the chambers, the air pressure inside the two sub-chambers, and the hydrodynamic pressures on the two curtain walls. In this section, the dual-chamber OWC model with the following dimensions are tested: the chamber widths $B_1 = B_2 = 0.325$ m, the curtain wall draft $d = 0.20$ m, the diameters of the orifices $D_1 = D_2 = 0.045$ m which corresponds to the

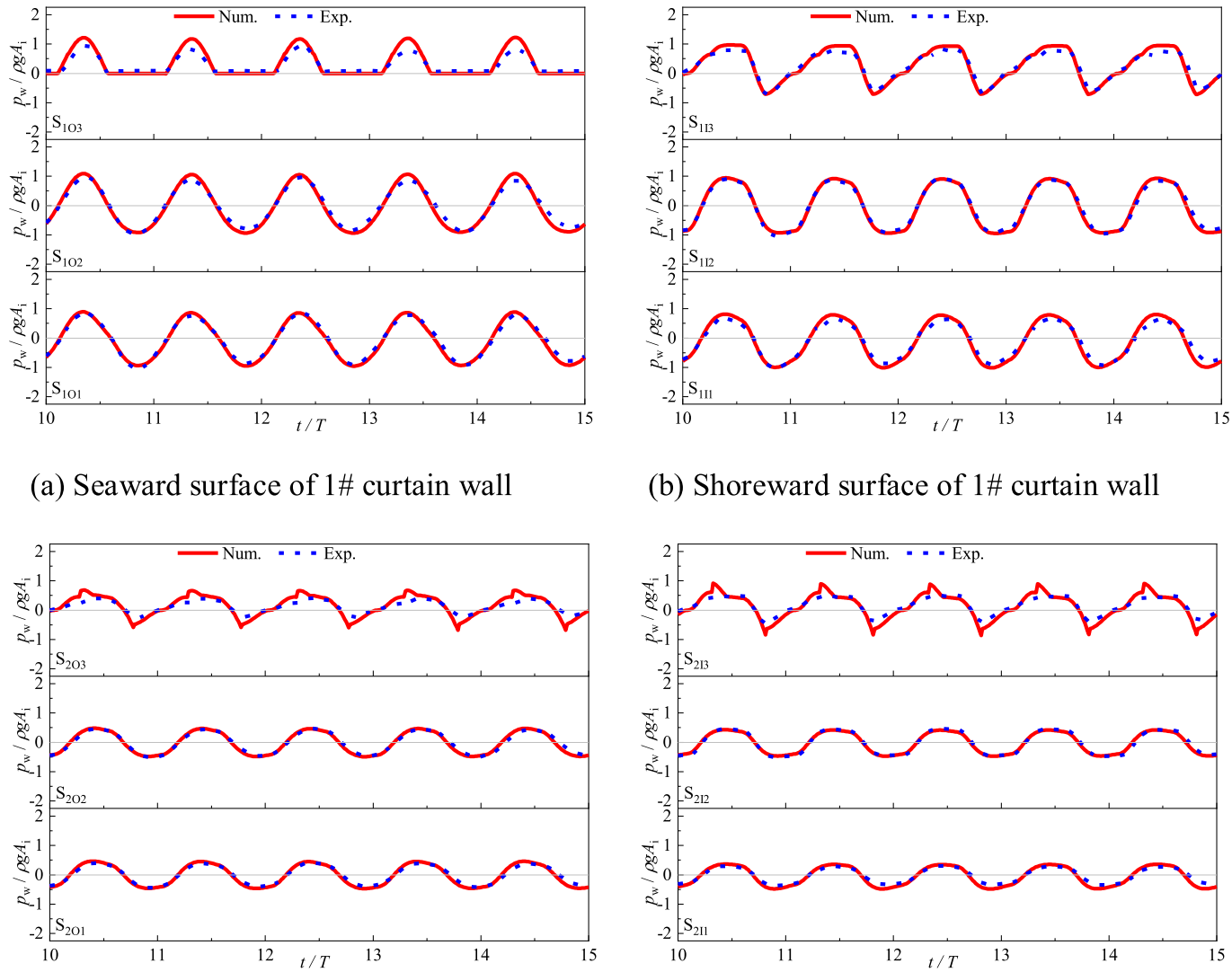

(a) Seaward surface of 1# curtain wall

(b) Shoreward surface of 1# curtain wall

(c) Seaward surface of 1# curtain wall

(d) Shoreward surface of 1# curtain wall

Fig. 8. Time histories of the hydrodynamic pressures on the (a) & (c) seaward and (b) & (d) shoreward surfaces of 1# (Upper) and 2# (Lower) curtain walls for $T = 1.9$ s ($kh = 1.29$).

widths of the slot sharp orifices used in 2-D numerical model of $B_{O1} = B_{O2} = 2.415$ mm.

The convergence of the numerical model was examined throughly in our previous studies on the hydrodynamic efficiency of identical dual-chamber OWC device (Ning et al., 2019), therefore, the same model parameters and mesh are used in the present study as follows: the mesh size and time step are set to $\Delta x = \lambda/30$ and $\Delta t = T/80$, respectively; the number of mesh segments at the surface boundaries of 1# and 2# curtain wall and the vertical boundaries of the wave flume are set to be 15 and 10, respectively; the simulation time is set to $30T$ to achieve at least 10 fully developed oscillation periods inside the dual-OWC chambers; the quadratic pneumatic coefficients of the two orifices are selected as $D_{dm1} = D_{dm2} = 1.0$ by comparisons with the experimental data; and the artificial viscous coefficients in 1# and 2# chamber are selected as $\mu_1 = 0$ and $\mu_2 = 0.12$, respectively.

Fig. 5(a) and (b) show the comparisons of the simulated and measured free-surface elevations at gauge G_1, G_2 and G_3 for $T = 1.2$ s ($kh = 2.81$) and 1.9 s ($kh = 1.29$), respectively. From the figures, it can be seen that the numerical model can capture the free surface variations very well. Fig. 6(a) and (b) show the comparisons of the predicted and measured air pressures in 1# and 2# chamber for $T = 1.2$ s and 1.9 s, respectively. As illustrated in Fig. 6(a), the air pressures in the chambers are over-predicted under the action of high frequency wave (i.e., $T = 1.2$ s, $kh = 2.81$). This is because the air compressibility effects become more evident due to the small surface motion inside the chamber under high-frequency short waves, which indicates that neglecting air compressibility may lead to some errors under a certain sea state (López et al., 2020). However, it should be noted that the observed air pressures inside the two sub-chambers are well predicted overall across the frequency range. As can be seen from Figs. 5 and 6, the free-surface elevation outside the chamber at wave gauge G_1 decreases, while the free-surface elevations at wave gauge G_2 and G_3 and the air pressures in the air chambers increase when the wave period increases from 1.2 s to 1.9 s. In addition, both the phase differences of free surfaces and air pressures in the two sub-chambers is reduced for larger wave period, leading to larger wave energy absorption.

Figs. 7 and 8 show the comparisons of the simulated and measured hydrodynamic pressures on the surfaces of two curtain walls for $T = 1.2$ s and 1.9 s, respectively. As can be seen from the top sub-figures in Figs. 7 and 8, both the predicted and measured pressure at the still water

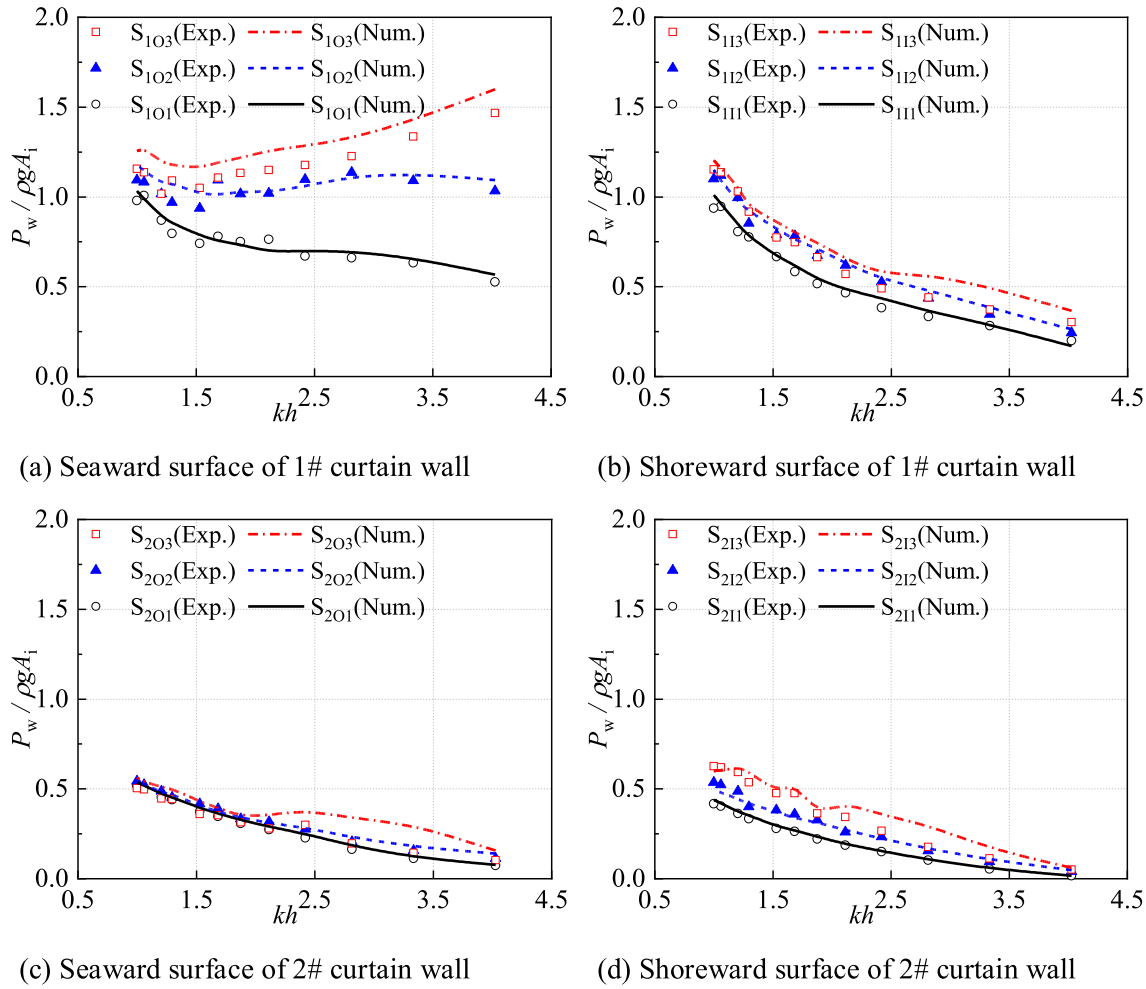

Fig. 9. Peak hydrodynamic pressure at 12 sensor locations on the seaward (Left) and shoreward (Right) surfaces of the 1# (Upper) and 2# (Lower) curtain walls.

Table 1
Average of the relative error between measured and predicted hydrodynamic pressure at the S_{1O1}~S_{2I3}. (%).

Position	S_{1O1}	S_{1O2}	S_{1O3}	S_{1I1}	S_{1I2}	S_{1I3}	S_{2O1}	S_{2O2}	S_{2O3}	S_{2I1}	S_{2I2}	S_{2I3}
$\bar{\sigma}$	4.06	5.63	9.50	3.85	4.36	6.17	4.47	3.96	12.72	4.27	5.76	7.66

level positions (i.e., S_{1O3}, S_{1I3}, S_{2O3} and S_{2I3}) show distorted and asymmetric behaviors due to the alternative actions of water and air at the wet and dry zone, which is not easy to be captured well by the potential numerical method. Although the wave pressures at these positions are overpredicted in some extent due to the complex air-water coupling, the overall agreement between the simulated and measured hydrodynamic pressures is quite good. Figs. 7 and 8 indicate that the hydrodynamic pressures on the curtain wall surfaces increase with wave period except that on the seaward surface of 1# curtain wall. Note that the total wave force exerted on the device does not necessarily increase with the wave period as discussed in the next section.

Fig. 9 shows the comparisons of the predicted and measured peak hydrodynamic pressure at the sensor positions on the two curtain walls. The averaged relative errors between the predicted and measured hydrodynamic pressure, $P_{w,exp}$ and $P_{w,num}$, at the curtain walls $\sigma = |P_{w,exp} - P_{w,num}|/P_{w,exp} \times 100\%$, are shown in Table 1. Due to the alternative actions of water and air at the wet and dry zone, the error of the pressure is relatively large at the still water level (i.e., S_{1O3}, S_{1I3}, S_{2O3} and S_{2I3}), but much smaller under the still water level. Overall, the numerical simulations are in a good agreement with experiments for the test cases.

The pressures on the seaward surface of 1# curtain wall decrease firstly and then increase with the dimensionless wave frequency *kh* as shown in Fig. 9(a). This is because high-frequency short waves are reflected by the 1# curtain wall due to weak transmission at high frequency while low-frequency long waves are reflected by the back wall with little effect from curtain walls. Whereas, as illustrated in Fig. 9(b), the pressures on the shoreward surface of 1# curtain wall decrease consistently with *kh* due to the fact that the wave energy transmitted into the 1# chamber decreases with *kh*. These behaviors are similar to those of the pressures on the front wall of a single-chamber OWC-WEC (Ning et al., 2016a). However, the pressures on both seaward and shoreward surface of 2# curtain wall decrease with increasing *kh*, or decreasing wavelength as shown in Fig. 9(c) and (d). This is due to the fact that the reflected wave energy increases with *kh* so that the wave transmitted into the chambers decreases in order to keep the total wave energy constant. Thus, compared with the wave pressures on 1# curtain wall, the pressure on 2# curtain wall is much smaller due to the sheltering effect of the 1# curtain wall. This will be discussed further in detail in the following section.

The aforementioned comparisons and analysis indicate that the present numerical model is capable to reproduce the processes of wave interactions with dual-chamber OWC device well. The wave induced

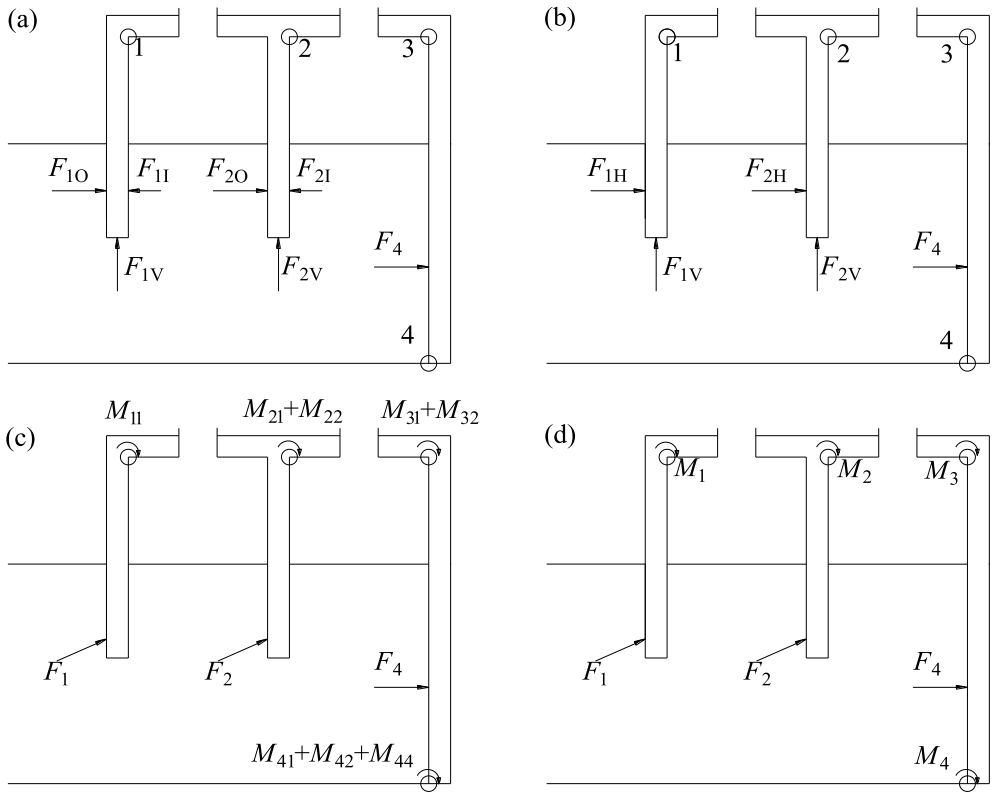

Fig. 10. Schematic of wave force and bending moment and 4 rotation centers on the dual-chamber OWC device: (a) components of the horizontal wave force and locations of the 4 rotation centers; (b) components of the total wave force; (c) components of the wave moment; and (d) total wave force and moment.

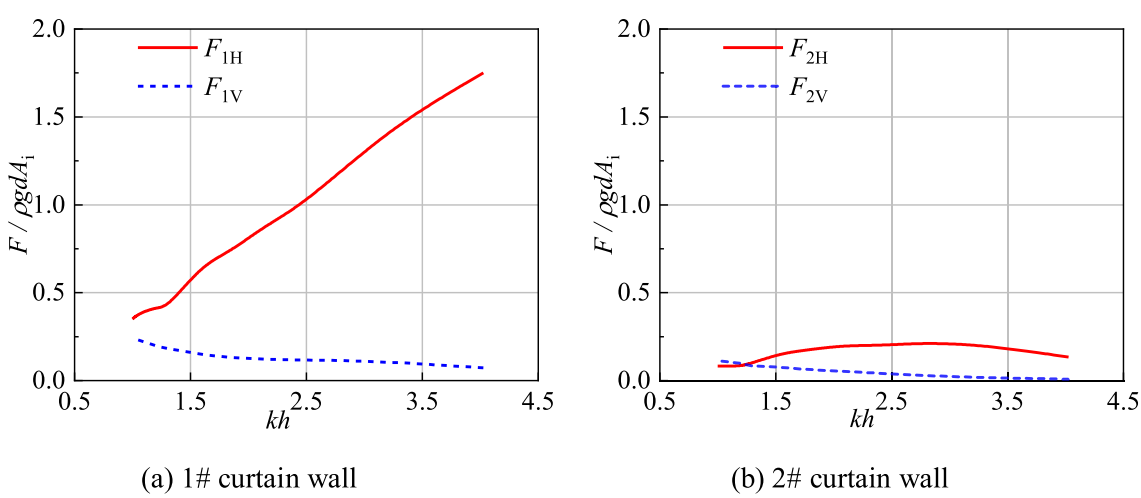

Fig. 11. Maximum horizontal and vertical wave forces on (a) 1# curtain wall and (b) 2# curtain wall versus *kh*.

dynamic pressure on the curtain walls is also well captured by taking air pressure inside the chambers and turbulence effects into account.

5. Results and discussions

5.1. Characteristics of wave force and moment

The diagrams of wave force, bending moment and 4 rotation centers on the dual-chamber OWC device are illustrated in Fig. 10. The dual-chamber OWC device can be divided into three cantilever structures, therefore, the inflection points 1, 2, 3 and 4 in Fig. 10(a) of the device are subjected to local maximum loads. These four points are taken as the rotational centers of wave bending moments. The wave force and bending moment can be obtained from Eqs. (7) and (8). F_{iV} denotes the vertical component of the wave force; F_{iO} and F_{iI} denote the seaward and shoreward surface components of the horizontal wave force on *i*# curtain wall (i = 1, 2), respectively. The total horizontal wave force on *i*# curtain wall F_{iH} (i = 1, 2) is the sum of the seaward and shoreward surface components:

$$F_{iH} = F_{iO} + F_{iI} \quad (i = 1, \ 2) \tag{9}$$

The total wave loading vector on *i*# curtain wall $\boldsymbol{F}_i$ (i = 1, 2) consists of the total horizontal and vertical components:

$$\boldsymbol{F}_i = F_{iH} \cdot \mathbf{i} + F_{iV} \cdot \mathbf{k} \quad (i = 1, \ 2) \tag{10}$$

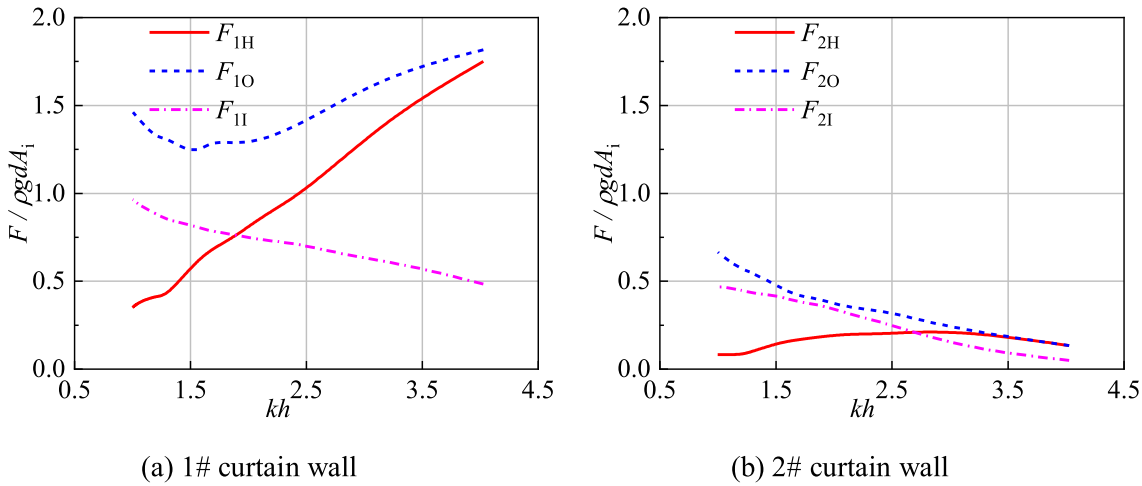

Fig. 12. Components of the horizontal wave forces on both surfaces of (a) 1# curtain wall and (b) 2# curtain wall. F_{iO} and F_{iI} ($I = 1, 2$): horizontal force acting on the seaward and shoreward surface of i# curtain wall; $F_{iH} = F_{iO} + F_{iI}$ ($I = 1, 2$).

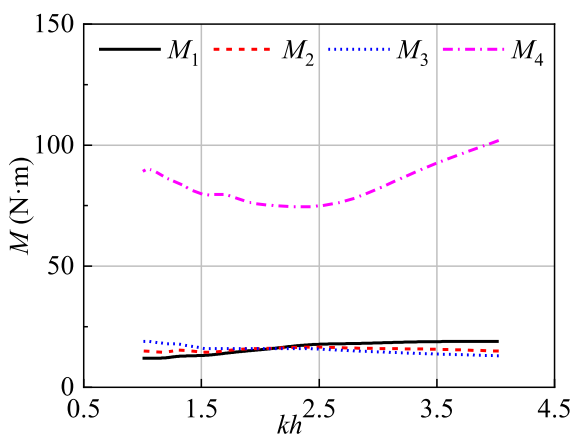

Fig. 13. Wave moments about the four rotation centers indicated in Fig. 10 versus kh.

in which $\boldsymbol{i}$ and $\boldsymbol{k}$ represent the unit normal vector in the x and z direction, respectively.

Wave force vectors $\boldsymbol{F}_1$ and $\boldsymbol{F}_2$ stand for the total wave forces on the 1# and 2# curtain wall, respectively. $\boldsymbol{F}_4$ denotes the total wave force on the back wall of the dual-chamber OWC device, which is equal to the horizontal component of the wave force because of zero vertical component on the back wall. The moment component $\boldsymbol{M}_{pj}$ represents the moment about rotation center p ($p = 1, 2, 3, 4$) by the wave force $\boldsymbol{F}_j$ ($j = 1, 2, 4$). For example, $\boldsymbol{M}_{42}$ represents the moment component about rotation center 4 due to the wave force $\boldsymbol{F}_2$ on 2# curtain wall. $\boldsymbol{M}_p$ denotes the total moment about rotation center p and is the sum of all moment components at the rotation center p. For example, $\boldsymbol{M}_4 = \boldsymbol{M}_{41} + \boldsymbol{M}_{42} + \boldsymbol{M}_{44}$.

5.1.1. Wave force

The geometrical parameters of dual-chamber OWC device are chosen as that in Section 4. Fig. 11(a) and (b) show the peak horizontal and vertical wave forces on 1# and 2# curtain wall, respectively. The peak wave forces F are normalized by $\rho g d A_i$. It can be seen that F_{1H} increases with the increase of dimensionless wave frequency kh, while F_{2H} increases gradually to a peak value first and then decreases with increasing kh. Furthermore, comparisons of Fig. 11(a) with Fig. 11(b) indicate that F_{1H} is much larger than F_{2H}. It follows that the seaside curtain wall, i.e., 1# curtain wall, suffered most of horizontal wave loadings. Thus, the strength of 1# curtain wall needs to be reinforced to ensure the structural safety of the device, whereas the strength of 2# curtain wall does not need to be as large as 1# curtain wall and less expensive material could be used to reduce construction cost. Additionally, as illustrated in Fig. 11(a) and (b), the vertical components of the wave forces are much smaller than the horizontal components, i.e., $F_{1V} < F_{1H}$ and $F_{2V} < F_{2H}$. This is due to the fact that the force bearing areas of vertical forces are much smaller than that of the corresponding horizontal forces because of the small thickness of curtain walls. Thus, for simplicity, only the horizontal wave forces are examined in detail in the present study, and the vertical wave forces are only considered in the wave moment calculation.

The maximum horizontal wave forces on two curtain walls, F_{1H} and F_{2H}, and its components, F_{iO} and F_{iI} ($i = 1, 2$) acting on the seaward and shoreward surface of the curtain walls are shown in Fig. 12(a) and (b), respectively. Note that the maximum horizontal wave forces F_H and its components (F_O and F_I) are computed independently due to the phase difference between them. The seaward surface component of horizontal wave force on 1# curtain wall, F_{1O}, firstly decreases and then increases with dimensionless wave frequency kh, while the shoreward surface component, F_{1I}, decreases monotonously with increasing kh. This is due to the fact that the majority of wave energy is transmitted through the curtain wall into the chambers and then reflected by the back wall owing to the negligible effect of curtain wall draft on low-frequency long waves. Therefore, the wave loading on both surfaces of 1# curtain wall is large. Thus, the shoreward surface component of the horizontal wave force F_{1I}, in the seaward direction, may cause structural damage from the chamber inner-side and should also be part of design consideration of OWC device. However, due to weaker wave transmission of shorter wave, the wave energy reflection by 1# curtain wall increases with the wave frequency. Consequently, the seaward surface component of horizontal wave force on 1# curtain wall increases, and the shoreward surface component decreases with kh in the high frequency region. As the sum of F_{1O} and F_{1I}, the total horizontal wave force, F_{1H}, increases with wave frequency. The characteristic of the wave force on 1# curtain wall of the dual-chamber OWC shows a similar trend as the wave force on the single-chamber OWC device front wall (Ning et al., 2016a).

However, the wave forces on 2# curtain wall behave differently due to different operation conditions of two curtain walls, i.e., 2# curtain wall protected by 1# curtain wall and waves not acting on 2# curtain wall directly. The horizontal wave loading on both surfaces of 2# curtain wall, F_{2O} and F_{2I}, decreases with wave frequency due to the sheltering effect of 1# curtain wall as shown in Fig. 12(b). As the sum of F_{2O} and F_{2I}, F_{2H} firstly increases with kh to its peak and then decreases with further increase of kh. Due to large transmission of low-frequency long waves and almost in-phase motion of two water columns inside 1# and

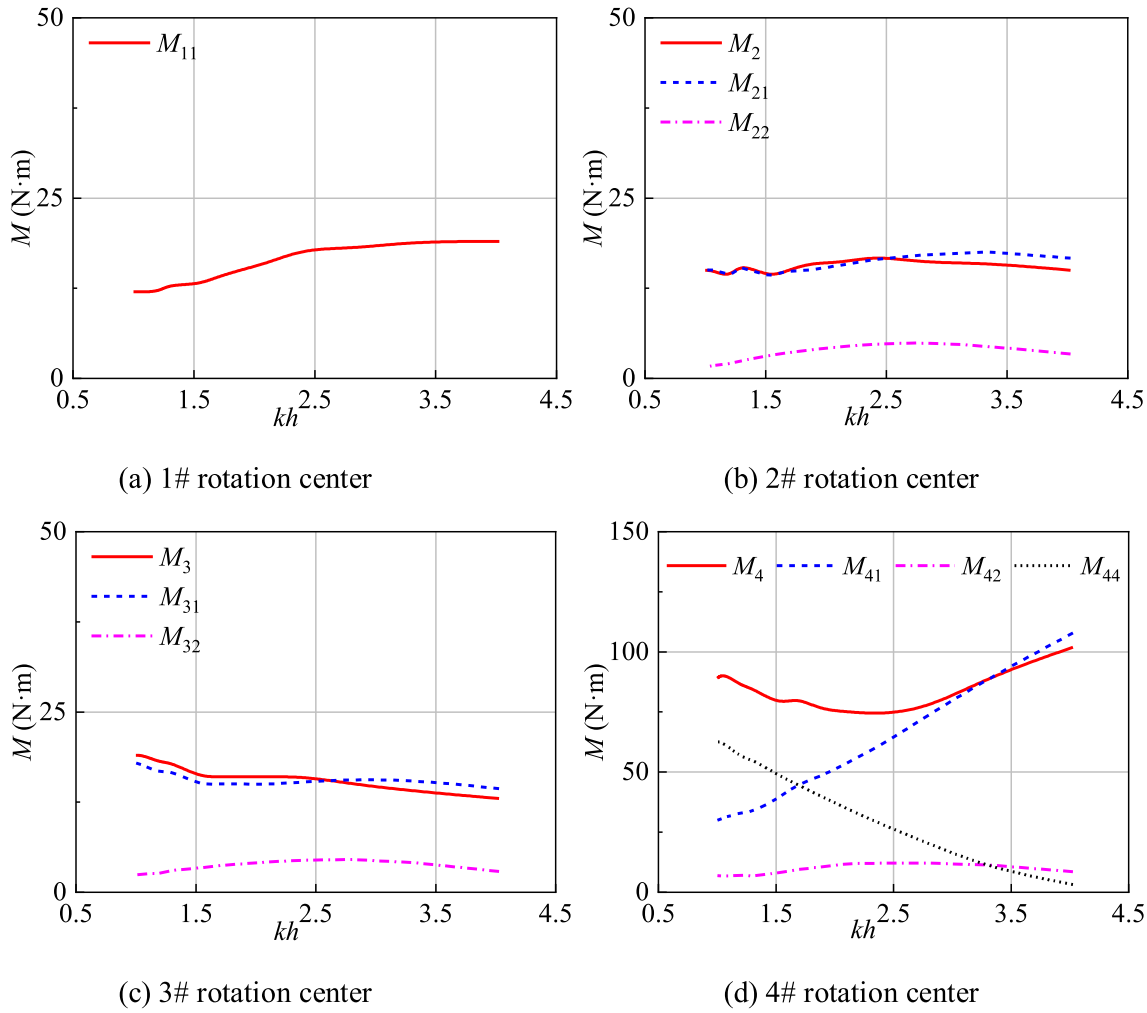

Fig. 14. Wave moment about the four rotation centers indicated in Fig. 10 and its components.

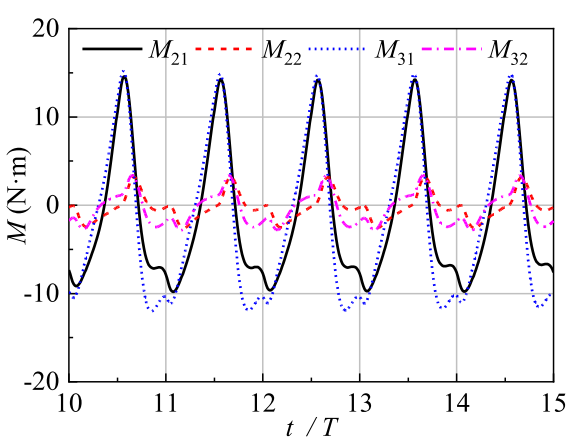

Fig. 15. Time histories of the wave moment components about 2# and 3# rotation centers for wave period $T = 1.70$ s ($kh = 1.53$).

2# chambers, F_{2H} is very small under low frequency waves. The phase difference between F_{2O} and F_{2I} increases with the wave frequency, thus F_{2H} increases with kh as a result. However, the wave transmitted into chambers decreases with increasing wave frequency. Thus, F_{2H} decreases with the further increase of kh after reaching its maximum.

5.1.2. Wave moment

Fig. 13 shows the wave moments about the four rotation centers, indicated in Fig. 10, as a function of dimensionless wave frequency kh. It is evident that the moment about rotation center 4, M_4, is much larger than that about the other three rotation centers, which suggests that the junction of back wall and seabed is the most vulnerable part of OWC system. Thus, the connection of back wall and seabed should be strengthened to avoid the device overturning. The largest moment occurs at rotation center 4 due to the fact that this position suffered all the wave forces as can be seen from Fig. 10. Additionally, it can be seen that M_4 firstly decreases with kh to its minimum and then increases with kh. This will be further discussed in the following text.

The moments and their components about the four rotation centers versus kh are shown in Fig. 14. The wave moment M_1 about 1# rotation center increases with kh as shown in Fig. 14(a), which is similar to the wave force on 1# curtain wall, F_1. This is due to the fact that M_1 only have one component M_{11} contributed by the wave force on the 1# curtain wall. For the wave moments M_2 and M_3, both of them have two components which are due to the wave forces F_1 and F_2 on 1# and 2# curtain walls, respectively, i.e., M_{21} and M_{22} for M_2 and M_{31} and M_{32} for M_3. It can be seen that F_1 is much larger than F_2, M_{21} is much larger M_{22} and M_{31} is much larger than M_{32} as shown in Fig. 14(b) and (c). To further verify the contributions of wave forces F_1 and F_2, Fig. 15 shows the time series of M_{21}, M_{22}, M_{31} and M_{32} for wave period $T = 1.70$ s (i.e., $kh = 1.53$). It can also be seen that the moments due to F_1 are much larger than those due to F_2 so that the wave moment is mainly due to F_1 and characteristics of M_2 and M_3 are mainly determined by M_{21} and M_{31},

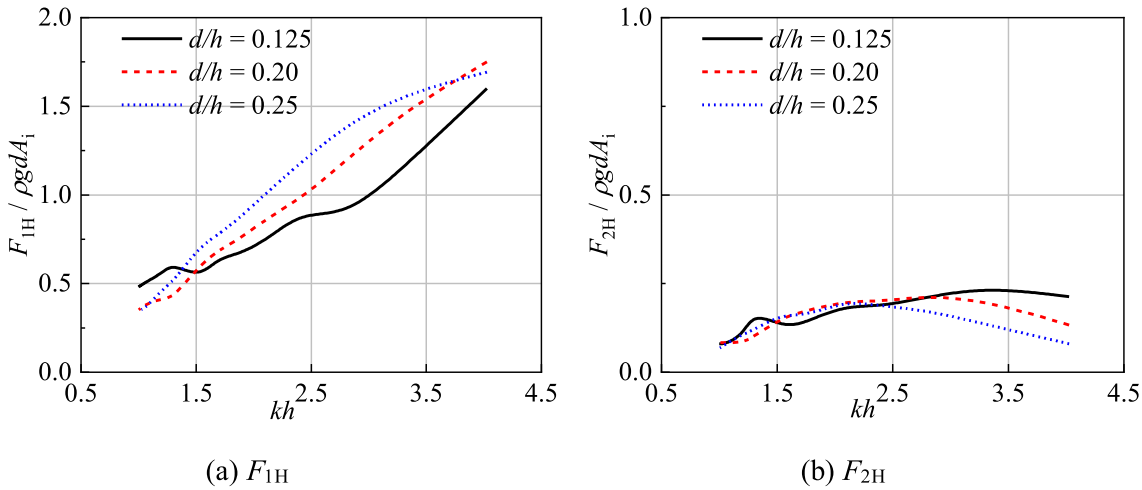

Fig. 16. Maximum horizontal wave forces on (a) 1# curtain wall and (b) 2# curtain wall for three different curtain wall drafts d/h = 0.125, 0.2 and 0.25.

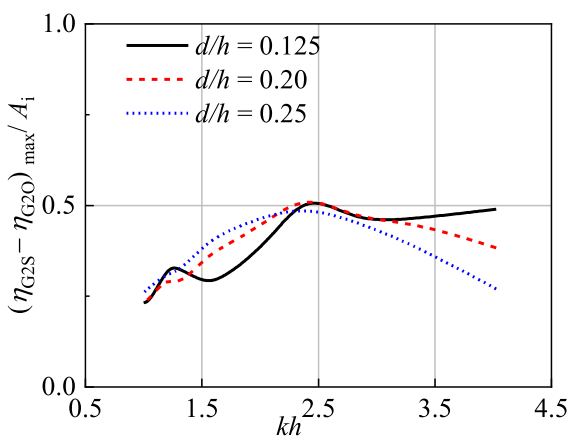

Fig. 17. The normalized free surface elevation differences between the two surfaces of 2# curtain wall versus kh for d/h = 0.125, 0.20 and 0.25.

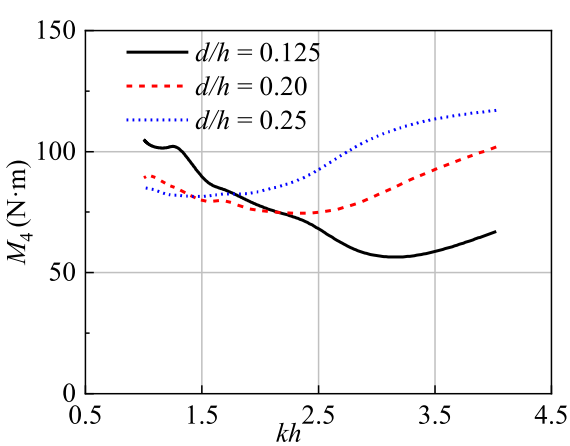

Fig. 18. Maximum wave moment about 4# rotation center for three different curtain wall drafts d/h = 0.125, 0.2 and 0.25.

respectively. Similar to F_1, M_{21} and therefore M_2 increase with kh. However, though M_{31} is also due to F_1, M_{31} no longer increases with kh, instead, it decreases with kh. As described before, F_1 is the sum of two components F_{1H} and F_{1V}, and the latter is much smaller than the former. However, for rotation center 3, the moment arm for F_{1V} is much larger than that for F_{1H}, and the moments due to F_{1H} and F_{1V} are in opposite direction. Thus, M_{31} and M_3 decrease with kh due to the increased effect of F_{1V} by the larger moment arm.

The moment about rotation center 4, M_4, has three components M_{41}, M_{42} and M_{44}. The moment component M_{42} due to F_2 still plays a very small role, while the moment components M_{41} due to F_1 and M_{44} due to F_4 play a main role in the M_4 as illustrated in Fig. 14(d). M_{41} increases with increasing kh and plays a dominant role in the high frequency region due to F_1 increasing with the wave frequency. In contrast, M_{44} decreases with kh and has a relative larger contribution, especially in the low-frequency long wave region. This is due to large transmission of long waves in the low frequency region, and the waves can easily enter the chambers and exert hydrodynamic force F_4 on the back wall of the device and finally produce a moment about the 4# rotation center. As the sum of its three components M_{41}, M_{42} and M_{44}, M_4 firstly decreases and then increases with kh. This indicates that the rotation center 4 suffered a relative larger moment at both low-frequency long waves and high-frequency short waves.

From the above discussion, the 4# rotation center suffered the largest moment. Based on structural mechanics, this position is also subjected to the largest shear force due to the large horizontal wave forces. In the real world, however, the connection of the OWC device and the seabed is a "U-shape" area instead of a point. Same as the Pico OWC wave power plant collapsed in a sea storm (Falcão et al., 2018), the moment about the 4# rotation center may cause overturning and failure of the device. Thus, in the following text, we will focus on the moment about 4# rotation center.

5.2. Effect of curtain wall draft

Effect of curtain wall draft on wave force and bending moment is of interest for design purposes. Three curtain wall drafts d = 0.125, 0.2 and 0.25 m (the relative drafts d/h = 0.125, 0.2 and 0.25) are examined with the chamber widths $B_1 = B_2 =$ 0.325 m and the orifice widths $B_{O1} = B_{O2} =$ 2.415 mm kept constants.

Fig. 16 shows the variation of the horizontal wave forces on the two curtain walls with kh for relative curtain wall drafts d/h = 0.125, 0.2 and 0.25. It can be observed that the horizontal wave forces are greatly influenced by the curtain wall draft. F_{1H} increases with the increase of curtain wall draft due to the increasing bearing area of 1# curtain wall as shown in Fig. 16(a). While F_{2H} remains almost constant regardless draft variation when $kh < 2.5$ and decreases with the increasing curtain wall draft d when $kh > 2.5$. This result is due to the fact that the barrier effect of the curtain walls is weak under low frequency long waves. Thus, the influence of curtain wall draft on wave force is very limited when $kh < 2.5$. However, when $kh > 2.5$, most incident waves are blocked by 1#

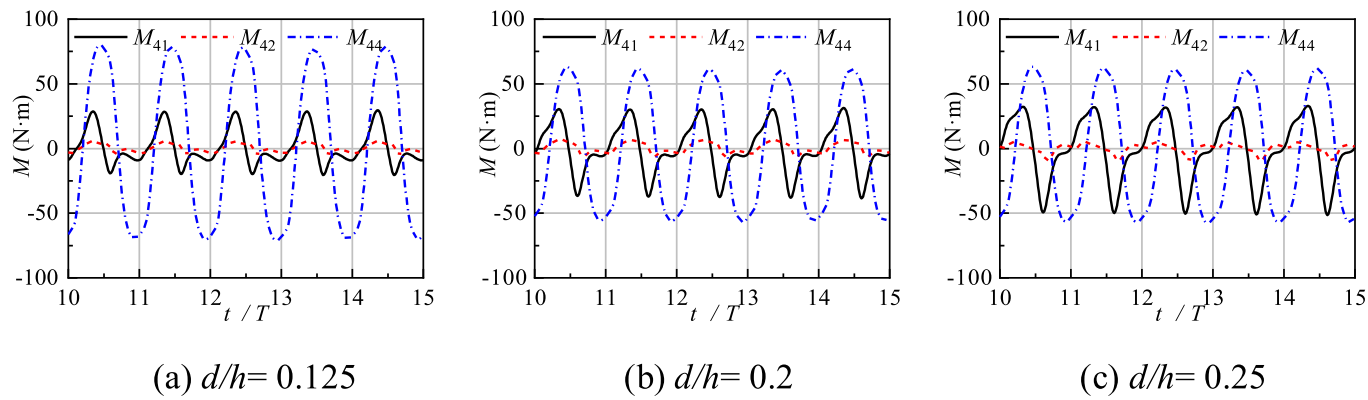

Fig. 19. Time histories of three components of wave moment M_4 about 4# rotation center for different curtain wall drafts at wave period T = 2.2 s (kh = 1.06).

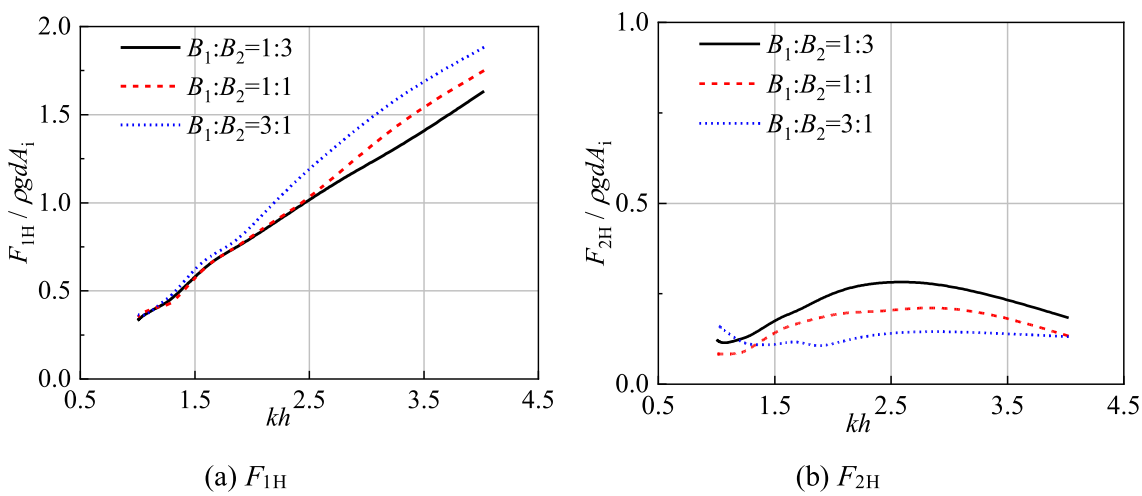

Fig. 20. Maximum horizontal wave forces on the (a) 1# curtain wall and (b) 2# curtain wall for three different sub-chamber width ratios B_1: B_2 = 1: 3, 1:1 and 3:1.

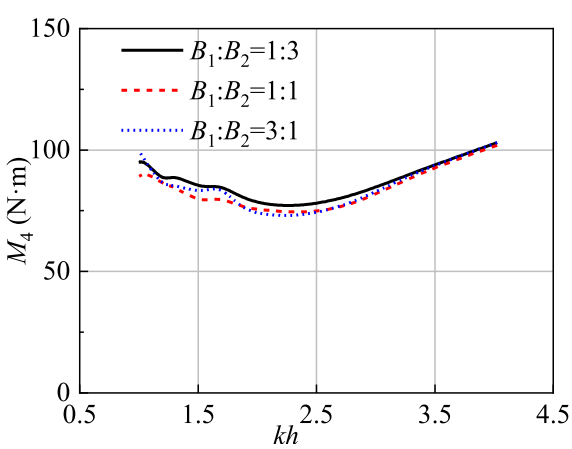

Fig. 21. Maximum wave moment about the joint of device and seabed (i.e., 4# rotation center indicated in Fig. 10) for three different sub-chamber width ratios B_1: B_2 = 1: 3, 1:1 and 3:1.

curtain wall outside the chambers due to weak wave transmission at high frequency regime and the wave blockage increases with the curtain wall draft. Therefore, the wave forces on 2# curtain wall decreases with curtain wall draft under high frequency wave actions as shown in Fig. 16 (b). The wave loading on the curtain wall is also dependent on the difference in the free surface elevation at its two surfaces. To illustrate the above phenomenon, the difference in the free surface elevation on the two surfaces of 2# curtain wall is shown in Fig. 17. The vertical axis (η_{G2S}-η_{G2O}) means the differences of the time histories of the free surface elevations, η_{G2S} and η_{G2O} are the free surface elevations at the seaward and shoreward surfaces of 2# curtain wall, respectively. Fig. 17 indicates that the free surface elevation difference (η_{G2S}-η_{G2O}) decreases with increasing curtain wall draft d. As a consequence, the total horizontal wave force on 2# curtain wall, F_{2H}, decreases with the increase of curtain wall draft d. It should be noted that F_{1H} is much larger than F_{2H}, thus, the wave force on 1# curtain wall is on the focus of the rest of the paper.

Fig. 18 shows the variation of wave moment about 4# rotation center (i.e., M_4) with kh for relative drafts d/h = 0.125, 0.2 and 0.25. It is evident that the wave moment M_4 increases with the curtain wall draft d for high frequency waves. This is due to the fact that the wave moment M_4 is mainly contributed by F_1 in the high frequency region according to Fig. 14(d). However, the opposite is true for the low frequency wave, i.e., the smaller the curtain wall draft, the larger the wave moment. To explain this phenomenon, the time histories of the three wave moment components (i.e., M_{41}, M_{42} and M_{44}) about 4# rotation center at T = 2.2 s (kh = 1.06) for three different curtain wall drafts are illustrated in Fig. 19. Though the component M_{41} due to F_1 has a considerable contribution to M_4, which increases with curtain wall draft, M_{44} is the largest one among the three components contributing to M_4 at the three given curtain wall drafts. Namely, the moment M_4 is mainly due to the wave loading on the back wall, F_4, instead of that on 1# curtain wall, F_1, under the action of low-frequency long waves. Additionally, wave energy transmission into the OWC chambers increases with decreasing curtain wall draft and, it follows that wave loading on the back wall, F_4,

and therefore the wave moment M_4 increases with the decrease of curtain wall draft under the action of low frequency waves.

Combining the above discussion with power capture efficiency consideration, one may conclude that increasing curtain wall draft, not only reduces power capture efficiency (Ning et al., 2019), but also enlarges the wave force and moment on the OWC structure. Thus, from this perspective, we would aim to design small curtain wall draft to achieve high capture efficiency and small wave loads. Nevertheless, there are many other design concerns, such as wave deformation, tide level and so on. In addition, the curtain wall draft can only be reduced to certain value so that the free surface remains higher than the toe of curtain wall, otherwise the OWC becomes inefficiency.

5.3. Effect of sub-chamber width ratio

Effect of sub-chamber width ratio on wave force and bending moment is also of interest. Three sub-chamber width ratios B_1: $B_2 = 1$: 3, 1: 1 and 3: 1 are examined while keeping the total chamber width $B_1 + B_2 + C = 0.7$ m and curtain wall draft $d = 0.2$ m constants. And the orifice widths are adjusted with the chamber widths by keeping the opening ratio α constant at 0.66% as described before.

Fig. 20(a) and (b) show the variation of horizontal wave forces on 1# and 2# curtain walls with kh for sub-chamber width ratio at B_1: $B_2 = 1$: 3, 1: 1 and 3: 1. It is evident that the wave force on 1# curtain wall, F_{1H}, remains almost constant regardless sub-chamber width variation when $kh < 2.0$, and it increases with sub-chamber width ratio B_1: B_2 when $kh > 2.0$. In another word, the horizontal wave force on 1# curtain wall can be reduced by moving the 2# curtain wall close to 1# curtain wall while keeping the total chamber width constant. However, the wave force on 2# curtain wall, F_{2H}, increases with decreasing sub-chamber width ratio B_1: B_2. Fortunately, F_{2H} is much smaller than F_{1H}, therefore, though F_{2H} is enhanced by small sub-chamber width ratio, F_{2H} is still much smaller than F_{1H}. Thus, a smaller sub-chamber width ratio is recommended for a dual-chamber OWC device.

To further verify that a smaller sub-chamber width ratio is a better choice, the variation of wave moment about 4# rotation center, M_4, with kh for sub-chamber width ratio at B_1: $B_2 = 1$: 3, 1: 1 and 3: 1 is shown in Fig. 21. It can be noted that the effect of sub-chamber width ratio on M_4 is limited, therefore, can be ignored. Additionally, our previous experimental investigation of power capture efficiency also indicates that the effect of sub-chamber width ratio on wave energy absorption is negligible (Ning et al., 2019). Therefore, a smaller sub-chamber width ratio is suggested by considerations of both energy conversion efficiency and dynamic force and moment. In this case, although the total energy conversion efficiency is not improved and the largest wave moment about the joint of device and seabed is not reduced, the maximum horizontal wave loading exerted on 1# curtain wall is effectively reduced.

6. Conclusions

Wave-induced force and bending moment have significant impacts on safety and stability of OWC device. Thus, accurate predictions of wave force and moment on the OWC are of great importance to the reliability and safe operation of OWC device. The wave force and moment on a dual-chamber OWC are systemically studied in the present study by using a full-nonlinear numerical model based on potential flow theory and HOBEM. Wave force and bending moment were calculated based on Bernoulli equation which was modified by taking the air pressure inside the chamber and turbulence effects into account and was solved with an acceleration-potential method. The present numerical model has been validated against the experimental data from free surface elevation, air pressure and hydrodynamic pressure. Though the hydrodynamic pressures on the still water level are overpredicted due to the alternative actions of water and air, generally, the predictions agree well with the measurements. The characteristics of wave force and moment were investigated. The effects of three curtain wall drafts (i.e, $d/h = 0.125$, 0.2 and 0.25) and three sub-chamber width ratios (i.e., B_1: $B_2 = 1$: 3, 1: 1 and 3: 1) on the wave loads were examined with the total chamber width kept constant at $B_1 + B_2 + C = 0.7$ m. The following main conclusions can be drawn:

- The horizontal components of the wave forces on the two curtain walls of a dual-chamber OWC are much larger than the corresponding vertical components for the small thickness of the curtian walls.
- Due to the sheltering of the seaside curtain wall (i.e., 1# curtain wall), the horizontal wave force on the inner curtain wall (i.e., 2# curtain wall) is much smaller than that on the former, i.e., $F_{1H} > F_{2H}$. F_{1H} increases with wave frequency and is mainly contributed from its component acting on the seaward surface of 1# curtain wall, F_{1O}. However, F_{1I}, the shorward surface components of F_{1H}, could even be larger than F_{1O} due to the large transmission and reflection of low-frequency long waves. Therefore, a damage could be caused from the chamber inner side and which should be avoided.
- The joint of device and seabed (i.e., rotation center 4) suffered the largest wave moment M_4, which contributed mainly from the wave force on 1# curtain wall F_1 for high-frequency short waves and the wave force on back wall F_4 for low-frequency long waves. As a consequence, rotation center 4 suffered a relative larger moment at both low-frequency long waves and high-frequency short waves. Note that, this bending moment may cause an overturning of the device, and thus, should be one of the major concern for structure design and construction of the device.
- Generally, a larger curtain wall draft d leads to a larger wave force on 1# curtain wall F_1, and a smaller wave force on 2# curtain wall F_2 due to the shielding of 1# curtian wall. For the bending moment M_4, it increases with the curtain wall draft d for high frequency waves due to the increasing F_1, while it decreases with d for low frequency waves due to the increasing wave loading on the back wall F_4. In addition, the power capture efficiency increases with deceasing curtain wall draft according to previous experimental studies of dual-chamber OWC device. Thus, a smaller curtain wall draft is recommended as long as no air leak from the bottom of the curtain walls.
- While for the sub-chamber width ratio B_1: B_2, the results show that though (1) the wave force on 2# curtain wall decreases with increasing B_1: B_2 and (2) the wave moment about rotation center 4 and the power capture efficiency are not sensitive to the variation of B_1: B_2, (3) the horizontal wave force, F_{1H}, on the seaside curtain wall, i.e., 1# curtain wall, increases with B_1: B_2 and attains its peak value at B_1: $B_2 = 3$: 1. Therefore, adopting small sub-chamber width ratio B_1: B_2 could reduce the peak horizontal wave force on the dual-chamber device.

Overall, the wave pressure, wave force and bending moment on OWC devices determine the safety, reliability and stability of the structure. The present numerical model is a robust design tool to predict these wave loads characteristics under non-breaking waves for OWC device of various geometry under a variety wave conditions.

Declaration of competing interest

The authors declare that they have no known competing financial interests or personal relationships that could have appeared to influence the work reported in this paper.

CRediT authorship contribution statement

Rong-quan Wang: Conceptualization, Methodology, Software, Validation, Investigation, Writing - original draft. **De-zhi Ning:** Conceptualization, Resources, Supervision, Writing - review & editing. **Qing-ping Zou:** Writing - review & editing.

Acknowledgements

This work is supported by the National Key R&D Program of China (Grant No. 2018YFB151905), National Natural Science Foundation of China (Grant Nos. 51679036 and 51761135011), Project Funded by China Postdoctoral Science Foundation (Grant No. 2019TQ0048).

References

Arena, F., Laface, V., Malara, G., Romolo, A., Viviano, A., Fiamma, V., Sannino, G., Carillo, A., 2015. Wave climate analysis for the design of wave energy harvesters in the Mediterranean Sea. Renew. Energy 77, 125–141.
Ashlin, S.J., Sannasiraj, S.A., Sundar, V., 2015. Wave forces on an oscillating water column device. Procedia Eng. 116, 1019–1026.
Boccotti, P., 2012. Design of breakwater for conversion of wave energy into electrical energy. Ocean Eng. 51, 106–118.
Deng, Z.Z., Ren, X., Wang, L.X., Wang, P., 2019a. Hydrodynamic performance of a novel oscillating-water-column breakwater with a horizontal bottom-plate: experimental and numerical study. Ocean Eng. 187, 106174.
Deng, Z.Z., Wang, C., Wang, P., Higuera, P., Wang, R.Q., 2019b. Hydrodynamic performance of an offshore-stationary OWC device with a horizontal bottom plate: experimental and numerical study. Energy 187, 115941.
Deng, Z.Z., Wang, L., Zhao, X.Z., Wang, P., 2020. Wave power extraction by a nearshore oscillating water column converter with a surging lip-wall. Renew. Energy 146, 662–674.
Didier, E., Neves, D.R.C.B., Teixeira, P.R.F., Dias, J., Neves, M.G., 2016. Smoothed particle hydrodynamics numerical model for modeling an oscillating water chamber. Ocean Eng. 123, 397–410.
Elhanafi, A., 2016. Prediction of regular wave loads on a fixed offshore oscillating water column-wave energy converter using CFD. J. Ocean Eng. Sci. 1 (4), 268–283.
Elhanafi, A., Macfarlane, G., Fleming, A., Leong, Z., 2017. Scaling and air compressibility effects on a three-dimensional offshore stationary OWC wave energy converter. Appl. Energy 189, 1–20.
Elhanafi, A., Macfarlane, G., Ning, D., 2018. Hydrodynamic performance of single–chamber and dual–chamber offshore–stationary Oscillating Water Column devices using CFD. Appl. Energy 228, 82–96.
Falcão, A.F.O., Gato, L.M.C., Sarmento, A.J.N.A., Brito-Melo, A., 2018. The Pico OWC wave power plant: its life from conception to closure 1986–2018. In: Advances in Renewable Energies Offshore: Proceedings of the 3rd International Conference on Renewable Energies Offshore. RENEW 2018), Lisbon, Portugal, pp. 475–483.
Falcão, A.F.O., Henriques, J.C.C., 2014. Model-prototype similarity of oscillating-water-column wave energy converters. Int. J. Mar. Energy 6, 18–34.
Falcão, A.F.O., Henriques, J.C.C., 2016. Oscillating-water-column wave energy converters and air turbines: a review. Renew. Energy 85, 1391–1424.
He, F., Huang, Z.H., 2014. Hydrodynamic performance of pile-supported OWC-type structures as breakwaters: an experimental study. Ocean Eng. 88, 618–626.
He, F., Leng, J., Zhao, X.Z., 2017. An experimental investigation into the wave power extraction of a floating box-type breakwater with dual pneumatic chambers. Appl. Ocean Res. 67, 21–30.
He, F., Zhang, H.S., Zhao, J.J., Zheng, S.M., Iglesias, G., 2019. Hydrodynamic performance of a pile-supported OWC breakwater: an analytical study. Appl. Ocean Res. 88, 326–340.
Hong, D.C., Hong, S.Y., Hong, S.W., 2004a. Numerical study of the motions and drift force of a floating OWC device. Ocean Eng. 31 (2), 139–164.
Hong, D.C., Hong, S.Y., Hong, S.W., 2004b. Numerical study on the reverse drift force of floating BBDB wave energy absorbers. Ocean Eng. 31 (10), 1257–1294.
Huang, Z.H., Xu, C.H., Huang, S.J., 2019. A CFD simulation of wave loads on a pile-type oscillating-water-column device. J. Hydrodyn. 31 (1), 41–49.
Iglesias, G., Carballo, R., 2014. Wave farm impact: the role of farm-to-coast distance. Renew. Energy 69, 375–385.
Iturrioz, A., Guanche, R., Armesto, J.A., Alves, M.A., Vidal, C., Losada, I.J., 2014. Time-domain modeling of a fixed detached oscillating water column towards a floating multi-chamber device. Ocean Eng. 76, 65–74.
John Ashlin, S., Sundar, V., Sannasiraj, S.A., 2016. Effects of bottom profile of an oscillating water column device on its hydrodynamic characteristics. Renew. Energy 96, 341–353.
Kamath, A., Bihs, H., Arntsen, O.A., 2015. Numerical investigations of the hydrodynamics of an oscillating water column device. Ocean Eng. 102, 40–50.
Konispoliatis, D.N., Mavrakos, S.A., 2016. Hydrodynamic analysis of an array of interacting free-floating oscillating water column (OWC's) devices. Ocean Eng. 111, 179–197.
Koo, W., 2009. Nonlinear time–domain analysis of motion-restrained pneumatic floating breakwater. Ocean Eng. 36 (9), 723–731.
Koo, W.C., Kim, M.H., 2007. Fully nonlinear wave-body interactions with surface-piercing bodies. Ocean Eng. 34 (7), 1000–1012.
Liang, B., Fan, F., Liu, F., Gao, S., Zuo, H., 2014. 22-Year wave energy hindcast for the China East Adjacent Seas. Renew. Energy 71, 200–207.
Liu, Y.Y., Yoshida, S., Hu, C.H., Sueyoshi, M., Sun, L., Gao, J.L., Cong, P.W., He, G.H., 2018. A reliable open-source package for performance evaluation of floating renewable energy systems in coastal and offshore regions. Energy Convers. Manag. 174, 516–536.
López, I., Carballo, R., Taveira-Pinto, F., Iglesias, G., 2020. Sensitivity of OWC performance to air compressibility. Renew. Energy 145, 1334–1347.
Medina-Lopez, E., Allsop, W., Dimakopoulos, A., Bruce, T., 2015. Conjectures on the failure of the OWC breakwater at Mutriku. In: Proceedings of Coastal Structures and Solutions to Coastal Disasters Joint Conference, Boston, Massachusetts, pp. 1–12.
Monk, K., 2015. Forecasting for Control and Environmental Impacts of Wave Energy Converters. Ph.D Thesis. Plymouth University.
Ning, D.-z., Wang, R.-q., Chen, L.-f., Sun, K., 2019. Experimental investigation of a land-based dual-chamber OWC wave energy converter. Renew. Sustain. Energy Rev. 105, 48–60.
Ning, D.Z., Shi, J., Zou, Q.P., Teng, B., 2015. Investigation of hydrodynamic performance of an OWC (oscillating water column) wave energy device using a fully nonlinear HOBEM (higher-order boundary element method). Energy 83, 177–188.
Ning, D.Z., Wang, R.Q., Gou, Y., Zhao, M., Teng, B., 2016a. Numerical and experimental investigation of wave dynamics on a land-fixed OWC device. Energy 115, 326–337.
Ning, D.Z., Wang, R.Q., Zou, Q.P., Teng, B., 2016b. An experimental investigation of hydrodynamics of a fixed OWC Wave Energy Converter. Appl. Energy 168, 636–648.
Ning, D.Z., Zhou, Y., Zhang, C.W., 2018. Hydrodynamic modeling of a novel dual-chamber OWC wave energy converter. Appl. Ocean Res. 78, 180–191.
Pawitan, K.A., Dimakopoulos, A.S., Vicinanza, D., Allsop, W., Bruce, T., 2019. A loading model for an OWC caisson based upon large-scale measurements. Coast. Eng. 145, 1–20.
Rezanejad, K., Bhattacharjee, J., Guedes Soares, C., 2015. Analytical and numerical study of dual-chamber oscillating water columns on stepped bottom. Renew. Energy 75, 272–282.
Rezanejad, K., Souto-Iglesias, A., Guedes Soares, C., 2019. Experimental investigation on the hydrodynamic performance of an L-shaped duct oscillating water column wave energy converter. Ocean Eng. 173, 388–398.
Sheng, W.A., 2019. Wave energy conversion and hydrodynamics modelling technologies: a review. Renew. Sustain. Energy Rev. 109, 482–498.
Simonetti, I., Cappietti, L., Elsafti, H., Oumeraci, H., 2018. Evaluation of air compressibility effects on the performance of fixed OWC wave energy converters using CFD modelling. Renew. Energy 119, 741–753.
Viviano, A., Musumeci, R.E., Vicinanza, D., Foti, E., 2019. Pressures induced by regular waves on a large scale OWC. Coast. Eng. 152, 103528.
Viviano, A., Naty, S., Foti, E., 2018. Scale effects in physical modelling of a generalized OWC. Ocean Eng. 162, 248–258.
Viviano, A., Naty, S., Foti, E., Bruce, T., Allsop, W., Vicinanza, D., 2016. Large-scale experiments on the behaviour of a generalised Oscillating Water Column under random waves. Renew. Energy 99, 875–887.
Vyzikas, T., Deshoulieres, S., Barton, M., Giroux, O., Greaves, D., Simmonds, D., 2017a. Experimental investigation of different geometries of fixed oscillating water column devices. Renew. Energy 104, 248–258.
Vyzikas, T., Deshoulieres, S., Giroux, O., Barton, M., Greaves, D., 2017b. Numerical study of fixed Oscillating Water Column with RANS-type two-phase CFD model. Renew. Energy 102, 294–305.
Wang, R.Q., Ning, D.Z., 2020. Dynamic analysis of wave action on an OWC wave energy converter under the influence of viscosity. Renew. Energy 150, 578–588.
Wang, R.Q., Ning, D.Z., Zhang, C.W., 2017. Numerical investigation of the hydrodynamic performance of the dual-chamber oscillating water columns. In: Proceedings of the Twenty-Seventh (2017) International Ocean and Polar Engineering Conference, San Francisco, California, USA, pp. 66–70.
Wang, R.Q., Ning, D.Z., Zhang, C.W., Zou, Q.P., Liu, Z., 2018. Nonlinear and viscous effects on the hydrodynamic performance of a fixed OWC wave energy converter. Coast. Eng. 131, 42–50.
Xu, C.H., Huang, Z.H., 2019. Three-dimensional CFD simulation of a circular OWC with a nonlinear power-takeoff: model validation and a discussion on resonant sloshing inside the pneumatic chamber. Ocean Eng. 176, 184–198.
Xue, M.-A., Chen, Y.-C., Zheng, J.-H., Qian, L., Yuan, X.-L., 2019. Fluid dynamics analysis of sloshing pressure distribution in storage vessels of different shapes. Ocean Eng. 192.
Xue, M.-A., Zheng, J.-H., Lin, P.-Z., Yuan, X.-L., 2017. Experimental study on vertical baffles of different configurations in suppressing sloshing pressure. Ocean Eng. 136, 178–189.
Zheng, S.M., Antonini, A., Zhang, Y.L., Greaves, D., Miles, J., Iglesias, G., 2019. Wave power extraction from multiple oscillating water columns along a straight coast. J. Fluid Mech. 878, 445–480.
Zhou, Y., Zhang, C.W., Ning, D.Z., 2018. Hydrodynamic investigation of a concentric cylindrical OWC wave energy converter. Energies 11 (4), 11040985.